

REPORT DOCUMENTATION PAGE

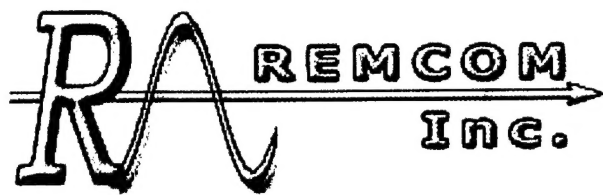
AFRL-SR-AR-TR-04

The public reporting burden for this collection of information is estimated to average 1 hour per response, including the gathering and maintaining the data needed, and completing and reviewing the collection of information. Send comments regarding this information, including suggestions for reducing the burden, to Department of Defense, Washington Headquarters Services, 1215 Jefferson Davis Highway, Suite 1204, Arlington, VA 22202-4302. Respondents should be aware that no penalty will be imposed for failing to comply with a collection of information if it does not display a currently valid OMB control number.

PLEASE DO NOT RETURN YOUR FORM TO THE ABOVE ADDRESS.

0524

1. REPORT DATE (DD-MM-YYYY) 19-08-2004	2. REPORT TYPE Final Technical Report	3. DATES COVERED (From - To) 15-05-2003 - 14-05-2004		
4. TITLE AND SUBTITLE Real Time RF Propagation Simulation Support		5a. CONTRACT NUMBER F49620-03-C-0037		
		5b. GRANT NUMBER		
		5c. PROGRAM ELEMENT NUMBER		
6. AUTHOR(S) Fast, Stephen A., Marston, C. Clay		5d. PROJECT NUMBER		
		5e. TASK NUMBER		
		5f. WORK UNIT NUMBER		
7. PERFORMING ORGANIZATION NAME(S) AND ADDRESS(ES) Remcom, Inc. 315 S. Allen Street Suite 222 State College, PA 16801-4850		8. PERFORMING ORGANIZATION REPORT NUMBER REM-PT-01		
9. SPONSORING/MONITORING AGENCY NAME(S) AND ADDRESS(ES) Air Force Office of Scientific Research 4015 Wilson Blvd. Room 713 Arlington, VA 22203-1954 <i>NM</i>		10. SPONSOR/MONITOR'S ACRONYM(S) AFOSR		
		11. SPONSOR/MONITOR'S REPORT NUMBER(S)		
12. DISTRIBUTION/AVAILABILITY STATEMENT Approved for public release; distribution is unlimited.				
13. SUPPLEMENTARY NOTES <i>20041021 011</i>				
14. ABSTRACT Recent research activities have been conducted to define the propagation and attenuation of communications signals through the atmosphere. These have, to a certain extent, allowed for the consideration of numerous factors, including multipath, ducting, diffraction, terrain, and weather phenomena. The Air Force Flight Test Center and the Navy Air Combat Environment, Test and Engineering Facility both require the capability to accurately represent the "real world" atmospheric propagation of communications signals for real-time Installed Systems Test Facility (ISFT) applications. This project developed methods for rapid efficient methods, algorithms and software to signal attenuation for the Joint Communications Simulator (JCS). The JCS is a real time simulator and thus the delivered software must provide propagation predictions for all relevant simulation players. Only those propagation predictions in which the loss displays a large change over a typical time step are evaluated. Thus, the terrain resolution and other first order environmental factors the determination of re-computation time for the simulation assets.				
15. SUBJECT TERMS Communications, Signals, Diffraction, RF Propagation				
16. SECURITY CLASSIFICATION OF: a. REPORT U b. ABSTRACT U c. THIS PAGE U		17. LIMITATION OF ABSTRACT UU	18. NUMBER OF PAGES 73	19a. NAME OF RESPONSIBLE PERSON Stephen A. Fast
				19b. TELEPHONE NUMBER (Include area code) 814-861-1299 ext. 260



Real Time RF Propagation

Simulation Support for

AFSOR

June 24, 2004

Prepared Under

Contract No. F49620-03-C-0037

By

Stephen Fast (PI) and C. Clay Marston

Remcom, Inc.

315 S. Allen St., Suite 222

State College, PA 16801

(814) 861-1299 x 260

(814) 861-1308 Fax

Table of Contents

1. Introduction.....	1
2. Status of effort.....	2
3. Terrain Multipath Electromagnetic Model.....	2
3.1. Definitions.....	3
3.2. Comprehensive Perspective (Overview) of Partial Diffraction Factors Relevant to Terrestrial Propagation.....	4
3.2.1. Discussion of irregular terrain diffraction sectors	5
3.2.2. Discussion of irregular terrain including portions of uniform elevation (smooth earth)	6
3.3. Extraction of Geodesic Paths.....	8
3.4. Designation of Diffraction Centers and Forward Propagation Shadows.....	13
3.5. Ray Path Construction and Total Loss Calculation for Arbitrary Field Point.....	19
3.5.1. Continuity of attenuation across shadow boundaries.....	20
3.5.2. Discussion of Generalities Introduced by Sub Geodesic Obstructions (profiles with shadows obstructions).....	22
3.6. Fused wedges	23
4. Results	28
5. Further Research	31
5.1. Adjustment of Excessive Loss for Multiple Knife Edge Attenuations and for Overlapping Shadow Boundaries	31
5.2. Performance Enhancements.....	36
6. Schedule	37
7. Spending Record	38
8. Personnel Support.....	39
9. Publications	39
10. Interactions/Transitions	39
11. New discoveries, inventions, or patent disclosures	40
12. Honors/Awards	40
13. Appendix – Earlier Progress Report.....	41
13.1. Accomplishments/New Findings	41
13.1.1. Baseline run times and model comparisons.....	41
13.1.1.1. Terrain extraction study	41
13.1.1.2. Validation comparisons	42
13.1.1.3. Run time comparisons.....	52
13.1.2. Proposed methods and algorithm.....	52
13.1.2.1. Derivation and Discussion	52
13.1.2.2. Comparison with other models	60
14. Bibliography	64

1. Introduction

Scores of research activities have been conducted in recent years as part of an attempt to define the propagation and attenuation of communications signals through the atmosphere. These have, to a certain extent, allowed for the consideration of numerous factors, including multipath, ducting, diffraction, terrain, and weather phenomena. However, while it is the case that RF propagation models can provide a characterization of the physical aspects of these signals, future projects will require realistic and real-time representations of communications signals with these physical aspects incorporated. The Air Force Flight Test Center and the Navy Air Combat Environment, Test and Engineering Facility both require the capability to accurately represent the "real world" atmospheric propagation of communications signals for real-time Installed Systems Test Facility (ISFT) applications.

This research effort is directed at the fulfillment of this demand through the accomplishment of the following tasks: Search of the available literature and models of these phenomena; identify those numerically efficient algorithms and models with application to the installed systems test environment; and lastly, specify and prototype a software module for incorporation into the existing communication simulator. The effort will maximally utilize existing research and modeling and further extend those efforts to the ISTF application.

Specifically this task will develop methods for rapid efficient methods, algorithms and software to signal attenuation for the Joint Communications Simulator (JCS). The JCS is a real time simulator and thus the delivered software must provide propagation predictions in real time for all relevant simulation players. The Test and Evaluation scenarios consist of a 400 x 400 square km battle space area in which the system under test is immersed. Every simulation player is moved on 1/20 second time steps producing a typical aircraft movement of 10 meters per time step. Since there are up to 400 mobile platforms and 2000 emitters in the scenario, this gives a potential required execution time for a single propagation prediction of no less than 1/80,000 seconds. The calculation time constraint includes not only determining the physical interactions, but also extraction of terrain data and other environmental data. Obviously, if possible, only those propagation predictions in which the loss displays a large change over a typical time step should be evaluated. Thus, the terrain resolution and other first order environmental factors will drive determining the re-computation time for the simulation assets.

The priorities for this research were coordinated with the JCS program manager and the developers. Their foremost concern is giving JCS the capability to model terrain effects. Initially the priority is for first order terrain effects caused by terrain blockage. Once the first order attenuation effects have been integrated, terrain multi-path is to be considered.

Because the JCS currently only computes free space loss without considering terrain blockage or reflection, the first phase of this research effort shall explore computational methods for Line of Sight (LOS) interference and Beyond Line of Sight (BLOS) diffraction effects. Further the JCS has only 96 signal generators available to model

multi-path signals, thus only the direct and a representative composite reflected ray will be used for the simulated communications link. In addition to improving LOS and BLOS methods, optimal methods to extract terrain data while determining propagation relevant geometrical properties shall be investigated. During this phase we intend to improve upon the accuracy and run time speed of the methods commonly found in the Joint Spectrum Center's (JSC) Terrain Integrated Rough Earth Model (TIREM) and the Institute of Telecommunications Service's (ITS) Irregular Terrain Model (ITM), also known as Longley-Rice. Parabolic Equation methods, unless implemented on signal processing hardware, have been deemed to be much too slow to be used for the JCS.

The second phase of the project seeks to extend the methods from phase 1 to be able to model multi-path. This will expand upon the single reflected ray method to give a more statistical representation of the multi-path. Although many methods are currently applied to model multi-path in signal simulations, the computation constraints will force the multi-path model to be very fast and use limited computer resources. Further the multi-path methods will not be able to utilize the JSC signal processing hardware.

In short, Remcom shall develop efficient methods to model terrain reflection and diffraction including multi-path. Operational software based on the model will be developed in order to provide JCS the capability of running faster than real time propagation predictions required by the test and evaluation scenarios.

2. Status of effort

This model will not only be used by the ISTF JCS, but also by the Air Force Intelligence Warfare Activity (AFIWC). Because the AFIWC requires a similar model with an extended frequency range to 500 KHz, AFIWC is funding the development of the LF and HF ground wave methods.

This report summarizes the accomplishments toward the goals of the first phase. Since the last status report in September, 2003, we have continued testing our methods and evaluating their performance in preparation for integration with the terrain extraction, and transition to the JCS architecture. The project plan is found in Section 6 and the spending curves found in Section 7.

The prototype of Remcom's new propagation model incorporating first order terrain effects has been completed. This model, referred to as the Terrain Multipath Electromagnetic Model (TMEM), is described in detail in the next section.

3. Terrain Multipath Electromagnetic Model

Existing propagation models force a tradeoff between run-time and accuracy. Models based on the parabolic equation (PE) such as APM and VTRPE provide good results, yet are computationally intensive. Other methods are quicker, such as those used by TIREM and ITM, but results less realistic.

Remcom has developed the Terrain Multipath Electromagnetic Model (TMEM) to fill the need for a propagation model that is fast enough for simulation, yet provides realistic results.

3.1. Definitions

Path Loss is defined as the log of the ratio of the power actually received at a specified antenna to that transmitted.

$$L = -10 \log_{10} \left(\frac{P_R}{P_T} \right)$$

The received power P_R may be expressed (MKSA units) as the product of the power density of the electric field at the receiver (watts/m^2) and the theoretical maximum aperture area available to the emitter which for a Herzian dipole is $\frac{\lambda^2}{4\pi}$

$$P_R = \left(\frac{E_R^2}{120\pi} \right) \left(\frac{\lambda^2}{4\pi} \right)$$

Where 120π is the free space impedance associated with propagation in a vacuum

$$Z = \sqrt{\left(\frac{\mu_0}{\epsilon_0} \right)}$$

for which

$$\mu_0 \epsilon_0 = \frac{1}{c^2}$$

and

$$Z = \sqrt{\left(\frac{\mu_0}{\epsilon_0} \right)} = \sqrt{\left[\left(4\pi 10^{-7} c \right)^2 \right]} = 120\pi$$

and the constant radiated power at the transmitter is the product of the corresponding power density and the full surface area of the sphere at radius r , the line-of-sight distance between transmitter and receiver.

$$P_T = \frac{E_T^2}{(120\pi)} 4\pi r^2$$

whence

$$L = -10 \log_{10} \left(\frac{\frac{E_R^2 \lambda^2}{120\pi 4\pi}}{\frac{E_T^2}{120\pi} 4\pi r^2} \right)$$

$$L = 10 \log_{10} \left[\left(\frac{\lambda}{4\pi r} \right)^2 \left(\frac{E_R^2}{E_T^2} \right)^2 \right] = -20 \log_{10} \left[\left(\frac{\lambda}{4\pi r} \right) \left(\frac{E_R}{E_T} \right) \right]$$

If received and transmitted fields are equal, the ratio of fields in the second bracketed expression is unity and the path loss reduces to the first bracketed term which defines the free space loss. The ratio of received to transmitted fields defines the attenuation factor, and it is the principle objective of terrestrial propagation to model the log of the attenuation factor in dB to obtain the loss over free space or excess loss.

In this proposal the diffractive effects defining the excess loss are modeled as products of two elementary forms including that for diffraction over irregular terrain and associated with diffraction by a perfectly absorbing knife edge and that for smooth earth propagation and modeled according to the numerically accessible methods of Norton [10]. The profiles will be subdivided according to the geodesic geometry of the terrain and each subdivision will be categorized according to which of the two elementary diffraction models it best conforms. The total loss will be defined as the product of partial attenuation factors resulting from these elementary assignments and of a functional form intended to achieve continuity as the various partial diffraction sectors are traversed. The following section will display the essential features of the terrain subdivisions according to elementary diffractive forms and will include examples with smooth earth terrain and an example consisting exclusively of irregular terrain features.

3.2. Comprehensive Perspective (Overview) of Partial Diffraction Factors Relevant to Terrestrial Propagation

The elementary diffraction forms discussed in the previous section may be identified by the presence of characteristic features of the geodesic geometry inherent in the terrain profile. As applied to geometrical optics, geodesic paths are the ray paths of shortest distance from a fixed transmitter to a receiver of arbitrary range and height along the terrain profile. The diffraction centers used to compute partial attenuation factors for both irregular and smooth terrain may be identified as the vertices of the discrete portion of the geodesic path or as end points of the tangent arcs accompanying terrestrial geodesic paths over uniformly elevated terrain. The (discrete) diffraction centers are accompanied by optical accessibility sectors within which unobstructed ray paths exist between the diffraction center and a field point confined to the sector. The angular bounds of the sectors may be defined such that they subdivide the vertical propagation plane into regions dominated by the defining diffraction center which is located at the intersection

of the ray paths defining its upper and lower limits. An example of the subdivided radial propagation plane for a path profile consisting exclusively of irregular terrain appears in Figure 1.

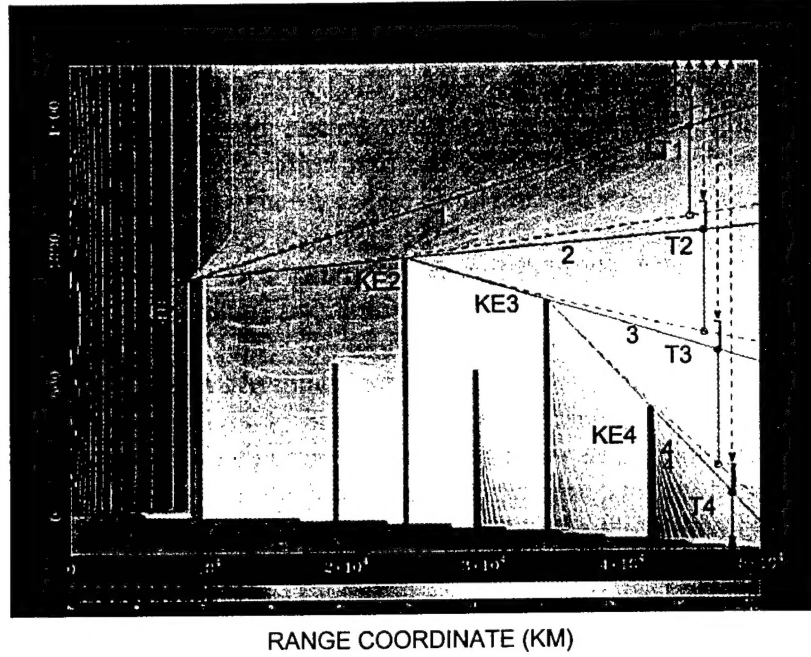


Figure 1. Subdivide Radial Propagation Plane for Irregular Terrain

3.2.1. Discussion of irregular terrain diffraction sectors

The terrain profile appearing in Figure 1, consisting of a random assortment of knife edges, will be used to illustrate the diffraction sectors described above by examining the functional behavior of the total path loss in a vertical excursion along the line segments appearing near the right margin of the figure. The total attenuation due to the knife edges is modeled as the product of single knife edge attenuations in which the effective source (transmitter) geometry is provided by the most immediate geodesic relation opposite the direction of propagation. The total loss is then the sum of the (partial) losses corresponding to each term in the product of attenuations.

A set of vertically arrayed symbols has been introduced in the figure for each diffraction sector to indicate the evolution of its partial excess loss contribution as a function of height. The diffraction sectors in Figure 1 have been labeled with the same Arabic numeral as that used to label the associated knife edge (diffraction center). The geodesic path to an arbitrary field point is a simple extension of the path to the diffraction center along a line segment from the diffraction vertex to the field point. The specific partial attenuation contributed by the sector depends upon the location of the field point relative to that sector. Thus the boundary between sectors 0 and 1 is marked by a solid line parallel to the shadow boundary of the first knife edge. Accompanying the solid line is a schematic representation of a curve of constant attenuation (shown as a dashed line) corresponding to the same excess loss as that evaluated at the first knife edge. Field points falling within sector (0) are assigned a partial excess loss equal to the standard

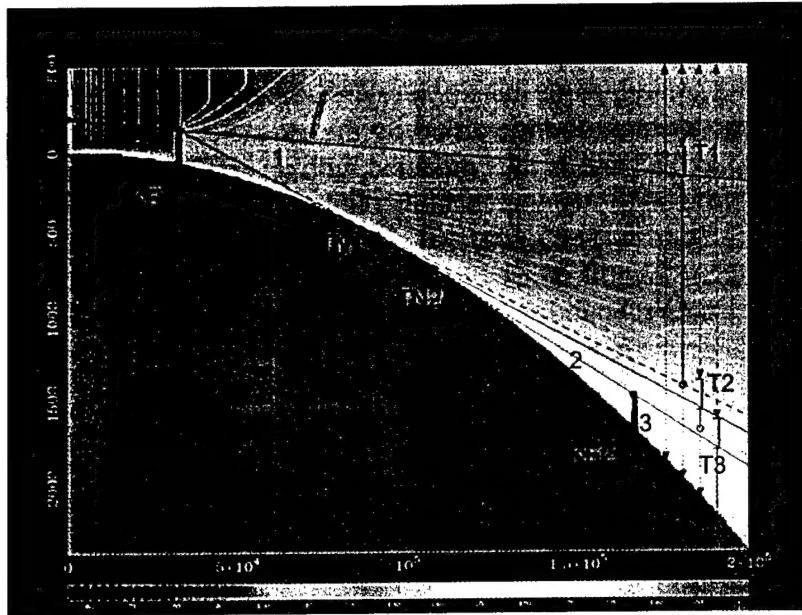
smooth earth attenuation loss, provided it does not exceed the value of the upper bound contour, and are otherwise assigned the value equal to that of the upper bound. Thus field points lying above the upper bound contour are assigned the standard smooth earth excess loss, whereas field points below the contour are assigned a constant excess loss which is the value defining the upper bound contour.

As the field point approaches the first sector, (which is dominated by single knife edge diffraction involving the transmitter and the terrain obstruction labeled KE1 in the figure), the contribution to the loss from the first knife edge is assigned a value of zero until the clearance ratio above the first knife edge exceeds a value of -0.78. The geometry corresponding to this transitional value of the clearance ratio is indicated in the figure by a square bracket labeled T1. (In addition, the geometry corresponding to a clearance ratio of -.78 is indicated for each sector by a like-numbered square bracket slightly above the respective shadow boundary.) Field points below the critical clearance ratio of transition region T1 are assigned partial losses given by the standard Fresnel integral for a perfectly absorbing knife edge [8], subject to an upper bound given by the loss computed at the next higher geodesic point. The value of the upper bound loss for each sector is shown in the figure as a dashed contour line near the lower bound of the sector and intersecting the corresponding following knife edge. As the vertical descent is continued a non-zero value of excess partial loss is contributed by each sector encountered, provided the clearance ratio exceeds -.78 and provided that it does not exceed this upper attenuation limit.

As the vertical descent enters the lowermost sector(4), the total excess path loss has accumulated a partial excess loss from each of the four sectors given by the upper attenuation limit of that sector and the final partial loss is that due to the fourth knife edge with effective source at the third diffraction center. The following section will examine a more general terrain configuration including a significant smooth earth component which will require elementary smooth earth diffraction methods to compute the corresponding partial diffraction contribution.

3.2.2. Discussion of irregular terrain including portions of uniform elevation (smooth earth)

A more general terrain profile including an optically significant portion of uniform elevation appears in Figure 2 and is further characterized by two non inter-visible knife edges. The diffraction sectors in the figure include that marked (0) above the shadow boundary of the first knife edge (KE1), sector (1) below the first shadow boundary and above the first tangent line passing through point TN1, sector (2) modeled by smooth earth diffraction, between the first and second tangent lines passing respectively through points TN1 and TN2, and finally that marked (3) which occupies the region below the shadow boundary of the second knife edge.



RANGE COORDINATE (KM)

Figure 2. General Terrain Profile with Two Non-Intervisible Knife Edges

An objective in the design of the current model is that it reduces to smooth earth attenuation in the absence of irregular terrain features. In order to accomplish the reduction to smooth earth attenuation in the absence of irregular terrain, field points located in sector zero are understood by default to sustain an initial loss due only to smooth earth attenuation. As the transition to sector one is approached, the smooth earth attenuation loss is restricted to an upper bound given by its value at the first diffraction center. Continuity across the sector boundary is accomplished by defining the smooth earth attenuation as its conventional functional value if less than the upper bound loss and to otherwise defines the loss as equivalent to the upper bound loss. Consequently, a partial excess loss given by the standard functional form is assigned for field points lying above the transition contour and points lying below the transition contour are assigned a partial loss equivalent to the its defining constant value.

As the boundary between sectors 0 and 1 is approached, an additional loss due to the knife edge labeled KE1 becomes significant as the clearance ratio above the first knife edge approaches the transition value of -0.78. The geometry along the second vertical line corresponding to this transition geometry is labeled T1 in Figure 2. The first sector is bounded below by the line passing through point TN1 which is the point of tangency with the smooth terrain. The contour corresponding to the limiting value of loss contributed by the first knife edge is schematically shown as a curved dotted line somewhat above the tangency. Below the transition region (T1)and within sector one, the partial loss contributed by the first knife edge is given by the conventional functional form if less than this upper bound value which is also the limiting value assigned for those losses otherwise exceeding the limit.

Continuing the vertical descent, as field points approach the tangent line through TN1, an additional loss attributable to attenuation by the encroaching smooth earth is expressed for points below the smooth earth transition region, labeled T2 in Figure 2. (The choice to use smooth earth attenuation is justified by the existence of smooth terrain between knife edges KE1 and KE2 and is thus modeled with an effective transmitter at the same height as the first knife edge and approaching a limiting value given by the loss evaluated at the second knife edge.) The additional smooth earth loss increases in value in the descent through sector 2 until it reaches its limiting value corresponding to the dotted contour above the shadow boundary of the second knife edge (KE2). Field points below the upper bound contour are assigned a partial diffraction loss equal to that defining the upper bound. A third partial diffraction loss due to the second knife edge (KE2) is sustained by those field points lying below the corresponding transition region T3 in Figure 2. This loss is supplemented by an additional shadowing loss modeled as a smooth earth attenuation of a previously knife edge diffracted field as discussed in the appendix (13).

3.3. Extraction of Geodesic Paths

Since the diffraction centers essential to the calculation of the path loss are confined to local geometrical convexities which define the geodesic path between relevant antennas, it becomes necessary to extract the relevant geodesic geometry intrinsic to the terrain profile. This section will describe a diffraction center identification process intended to avoid a possible oversight of similar methods which may ignore terrain features not among the vertices of the dominant geodesic path but optically relevant to the calculation.

Although the dominant diffraction centers are the vertices of the geodesic path between transmitter and receiver, the loss calculation may be significantly affected by sub-geodesic points, especially those within a Fresnel zone of the dominant geodesic ray paths. Restricting the optically relevant environment to the external geodesic path may lead to discontinuities in path loss calculation because the evolution of the terrain may introduce dramatic alterations of the points comprising the dominant geodesic path, permitting an erroneous neglect of optically significant terrain features no longer among the dominant geodesic vertices. Inclusion of sub-geodesic paths assures that points originally dominant in an evolving terrain profile may continue to exert their influence as the path is extended.

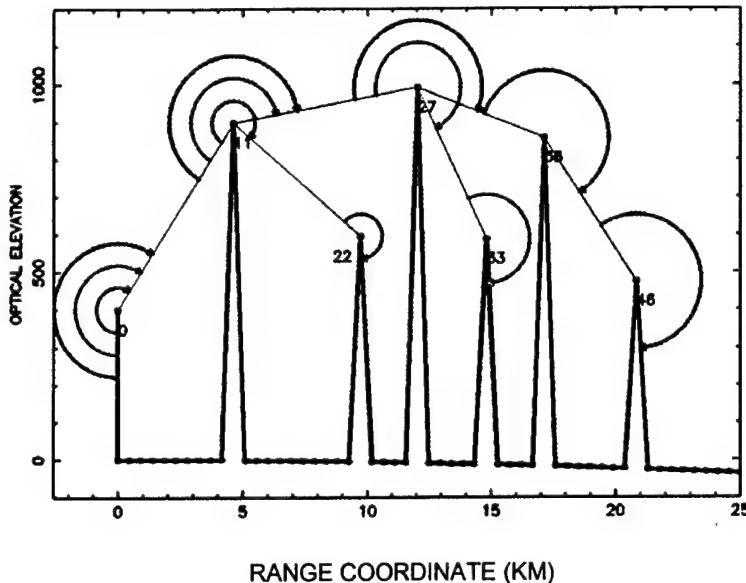


Figure 3. Delineation of Geodesic Ray Paths

As an example, consider the terrain profile appearing in Figure 3 which consists of a random assortment of five knife edges distributed over a 25 km path. Critical terrain points of this profile have been labeled by the order they appear within the profile. Terrain points labeled (0), (11), and (22), marked with red arcs, are the dominant geodesic points for the first 10 km of the path, but point (22) is excluded from the new set of dominant geodesic points which results if the path is extended to point (27) which replaces point (22) as the third point of the resulting dominant path marked with green circles.

A branching of geodesic paths is implied from point 11 of the first geodesic path to point 27 which is the first unique point of the second geodesic path, marked in green, which is then extended to point 33. This structure of the dominant geodesic path remains intact for paths of a lesser range coordinate than profile point 38 where a second branching from point 27 occurs to access the first unique point of the outermost geodesic path marked with blue arcs. Since the first set of optical paths marked with red and green arcs conform to the definition of optically relevant points for the shorter paths, a generalization of optical relevance would include all points considered optically relevant anywhere along an exhaustive traversal of the entire path profile. Defining points contained in a continuous geodesic (convex) path originating at the transmitter as elements of a geodesic seam regardless of length, the optically relevant points may be defined as all points lying on the geodesic seams generated by the specified invariant transmitter. Thus each of the three paths discussed above originate at the transmitter, define a locus of continuous convexity, comprise a geodesic seam and are therefore included among a universal set of optically relevant points, as defined here.

The geodesic seams are located by recording the indices of the geodesic path to a specified point on the path profile as a function of the range coordinate of that point. The geodesic paths are characterized by monotonically decreasing slopes and are therefore of

a negative second derivative. The relevant geometry for geodesic path extension inspection is depicted in Figure 4, where it is understood that final two points of a known geodesic path, labeled I0 and I1, have already been established. Inspection of the point at I2 for its suitability as an extension of the known geodesic path also requires knowledge of the point just beyond point I2 and shown as I3 in the figure. The continuity of negativity requires that the curvatures of the approach and exit vectors associated with point I2 are both negative. (The vector r_{01} from point (0) terminating at point (1) can be used to define mutually orthogonal unit vectors $e_1 = \hat{r}_{01}$ and e_2 as $k \times e_1$. The orientation of r_{12} with respect to \hat{r}_{01} is negative in the formal sense that $r_{12} \cdot e_2 < 0$. Alternatively the sign of the curvature may be defined as the sin of angle $\angle(I0-I1-I2)$ which is critically negative if it exceeds π) This requires that the approach angle to (I2), $\angle(I0-I1-I2)$, terminating on the point in question, and the exit angle $\angle(I1-I2-I3)$, centered on the point in question, must both be negative. Confirmation of both negative slopes justifies the inclusion of the point (I2) as a convex extension of the geodesic path whose current leading element is point I1.

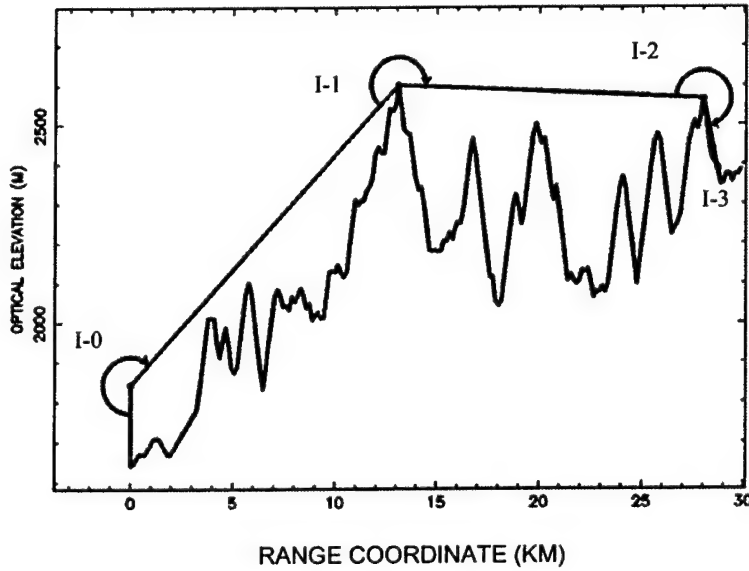


Figure 4. Geodesic Path Extension

For computational purposes, the proper curvatures of approach and exit are confirmed for each additional extension point and the process is repeated until a point is found which violates the continuity of negativity. If the point in question is found to exhibit a negative approach angle but a positive exit angle, it is recognized as being the non convex terminus of the current geodesic path and is discarded from further consideration. If the point however is found to exhibit a positive approach angle, the current path is terminated but the inspected point is retained for possible insertion into a higher order geodesic path. The laminated structure of the geodesic seams assures that a new geodesic path to such an excluded point may be established from a point within the current outermost geodesic path.

As exemplified in Figure 3, the first (red) geodesic path terminates at point (22) and a new geodesic path is initiated at point (27) as an extension from previous point (11) which is the last point among those of the previous geodesic path to satisfy the double negative curvature constraint for points (0, 11 27, 28) serving as (I0, I1, I2, I3) respectively. Points 1-10, 12-21 and 23-26 are eliminated in this process because none are properly configured to provide negative exit curvature when considered as extensions of any previous geodesic point. Continuing the analysis beyond point 27, points 28-32 are eliminated because ,although each as point I2 admits to a negative approach curvature from points (I0, I1; I2, I2 + 1) = (11, 27; I2, I2 + 1), none is properly configured with respect to the corresponding following point at I3 = I2 + 1 to provide the requisite negative exit curvature. An extension is found at point 33 which exhibits the proper approach and exit curvatures as defined by the vector relations of point (I0, I1; I2, I3) = (11, 27; 33, 34) respectively. No suitable extensions among the points 34-37 are found because, although each exhibits the desired approach curvature, each also exhibits an undesirable exit curvature when approached form point 33. Since the approach curvature to point 38 from {I0, I1; I2 I3} = (27, 33; 38, 39} is positive, the geodesic path is terminated, a new branch point from the previous geodesic path at point 27 is identified and the third and final geodesic path is extended beyond point 38 to its final extension at point 46.

The methods described above for irregular terrain are directly applicable to portions of the profile determined to be of uniform elevation as expected at sea level. The upper right panel of Figure 5 exemplifies a terrain profile consisting of irregular features, manifested here as knife edges at points (318) and (399) and of an extended portion of uniform elevation between the transmitter at point (0) and point (315). Extension of the geodesic path beyond point 0 involves examining approach and exit slopes of (I0, I1, I2, I3) for I2 beyond 0. (Points I0 and I1 are formally initialized as lying at the base and apex of the transmitter which is assigned terrain index 0) Points 1-108 are excluded because they each exhibit positive exit slope despite the negative approach curvature from point 0. Point 109 is the first point beyond the smooth earth horizon of point (0) and is also the first point to exhibit a negative exit curvature in the approach from point 0 and therefore the first extension of the geodesic path. The ray path from point (0) to its horizon at point (109) may be described as the tangential insertion of the ray path from the transmitter at point (0) into the geodesic path extended by a smooth earth arc beginning at point 109. When restricted to uniformly elevated terrain beyond an elevated point of a ray path, the search for path extensions with continuous negative curvature has then led to the detection of the horizon of the elevated terrain point.

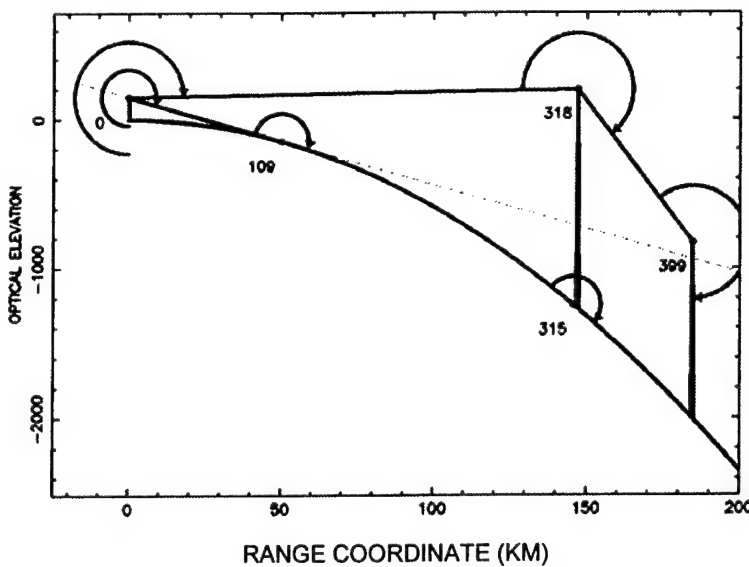


Figure 5. Smooth Earth with Inter-Visible Knife Edge

Upon tangential insertion into the uniformly elevated portion of the profile, here at the horizon point (109), all subsequent points satisfy the criterion of extended geodesic curvature until irregular terrain is encountered at point (318). Responding as described earlier to a detection of obstructed geodesic geometry, a search is conducted among the established geodesic points for a branch point to this first unique point of the next higher order geodesic path. From an inspection of points previous to point 318 for the proper approach and exit slopes, it becomes apparent that point 0 serves as the branch point to the next higher order geodesic path and that point 318 is the first unique point of the path which has been marked in green in the figure. The branching point is at point (0) because the knife edge at point (318) is above the projected horizon of point 0 shown in the Figure 5 as an extended tangent intersecting the transmitter horizon at point (109).

A variation of this geometry is shown in Figure 6 in which the first knife edge is now below the projected horizon of the transmitter. As with inter-visible obstructions separated by smooth earth discussed earlier, the first geodesic path proceeds from the transmitter at point (0) to its horizon which for this profile is now at point 127 and along the smooth earth arc to the first obstruction at point 396. The first geodesic path is terminated and a search is conducted for proper branching to a higher order geodesic path as before. It becomes apparent from the resulting inspection of points that point (219), beyond the first tangential insertion at point (127) and also a point within the uniformly elevated portion of the terrain, is the last point among those inspected which satisfies the curvature requirements for geodesic extension. The branching from point 219 is the greater terminus of the smooth geodesic arc between points 127 and 219, each of which is a tangential insertion focus and local (smooth earth) horizon for the corresponding irregular terrain features.

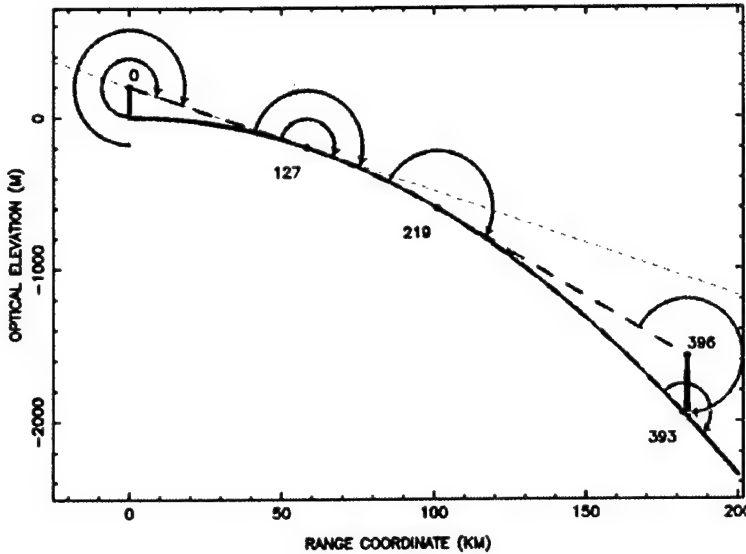


Figure 6. Knife Edge Beyond Horizon

3.4. Designation of Diffraction Centers and Forward Propagation Shadows

Provided the geodesic seams of the terrain profile, the diffraction centers may be identified according to a methodology described in this section. It is customary to minimally require that terrain vertices to be modeled as diffraction centers must block the direct Line of sight ray path between an emitter and other portions of the terrain. The geodesic seams identified in the previous section consist of serialized lines segments between adjacent vertices of the optical ray path and, for those paths encountering smooth earth profiles, continuous geodesic arcs of uniform elevation bounded by transitional tangent rays from both endpoints to the corresponding irregular terrain relation.

The geodesic seams provide the vertices of the discrete portions of the optical ray as well as any continuous geodesic segments introduced by portions of terrain determined to be of uniform elevation. Since the points of the geodesic path necessarily exhibit continuity of negative curvature, they also satisfy the earlier requirement of successive ray path obstruction. The vertices of the discrete portion of the geodesic seams appear to then qualify as centers of diffraction which for the purposes of this report are modeled as perfectly absorbing knife edges. The continuous portions of the ray paths, as exemplified by the arc between points (127) and (219) in Figure 6, and their most immediate irregular relations, as exemplified by points (0) and (396) in the Figure 6, define elements consisting of effective antennas of finite height separated by uniformly elevated terrain and may therefore be modeled as localized smooth earth attenuation partial diffraction factors.

According to the identification procedure thus described, the diffraction centers of the example profiles shown in Figure 7, Figure 9, and Figure 11 are identified respectively in Figure 13 - Figure 15 in which the knife edge diffraction centers of the discrete geodesic portion are indicated by the knife edge attenuation label AKE(IL, I0, IG) where the three

integer arguments reference the ordering of points in the geodesic path serving as effective source, diffraction center and limiting field point, respectively. The smooth earth attenuation diffraction centers are indicated in Figure 14 and Figure 15 by the smooth earth attenuation label ASE(I0, I1, I2, I3) in which the integer arguments indicate geodesic indices of points serving respectively as source, first and second tangents, and limiting attenuation field point. The effective transmitter geometry for the partial diffraction losses due to the knife edge at point (II-3) is defined by the geodesic path just preceding the knife edge, which in Figure 15 is point (II-2). Partial losses contributed by this knife edge are then computed with an effective transmitter located at point (II-2) which serves as the tangential origin of the ray path from the smooth earth to the knife edge at point (II-3).

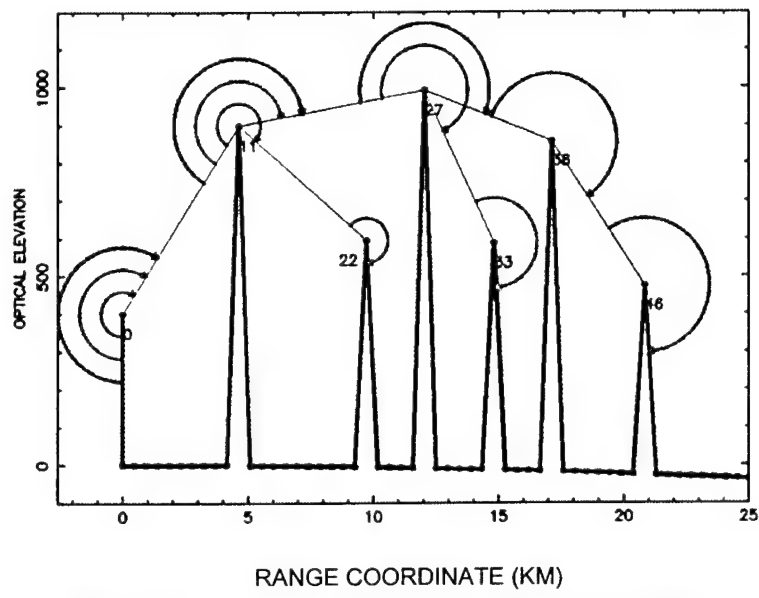


Figure 7. Delineation of Geodesic Ray Paths

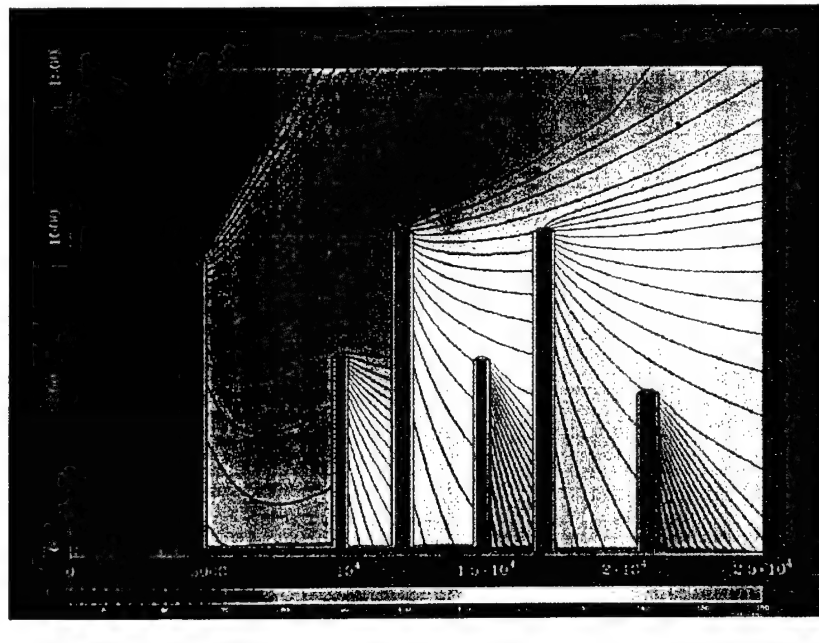


Figure 8. TMEM Propagation Calculation at 20.08 MHz

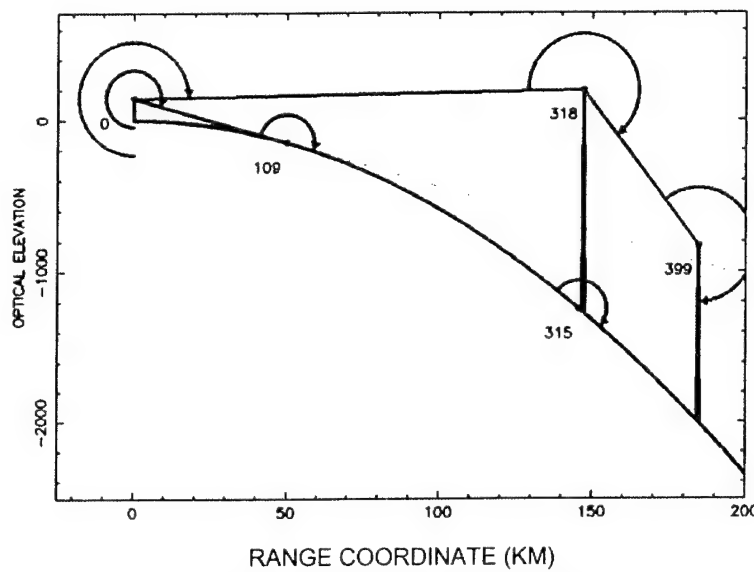


Figure 9. Smooth Earth with Inter-Visible Knife Edge

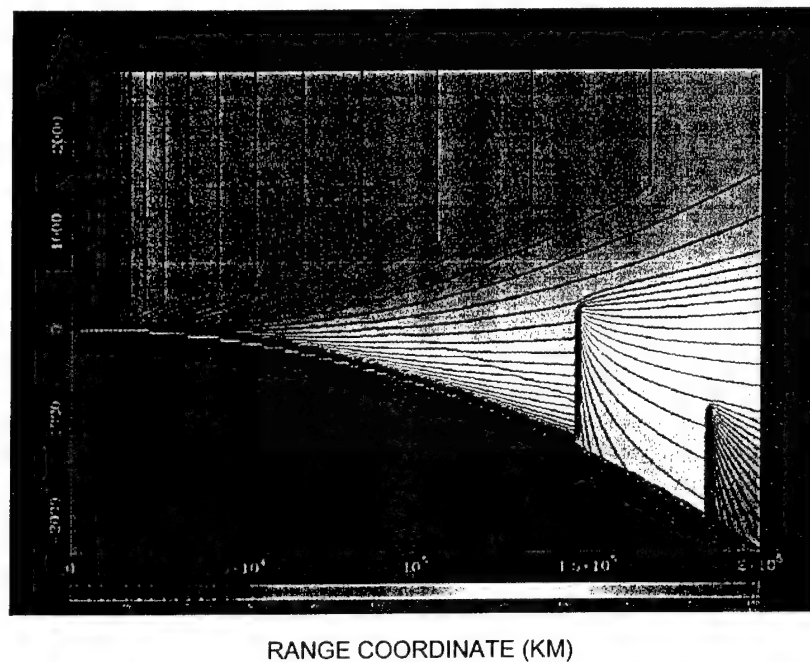


Figure 10. TMEM Smooth Earth Inter-Visible Knife Edge at 20.08 MHz

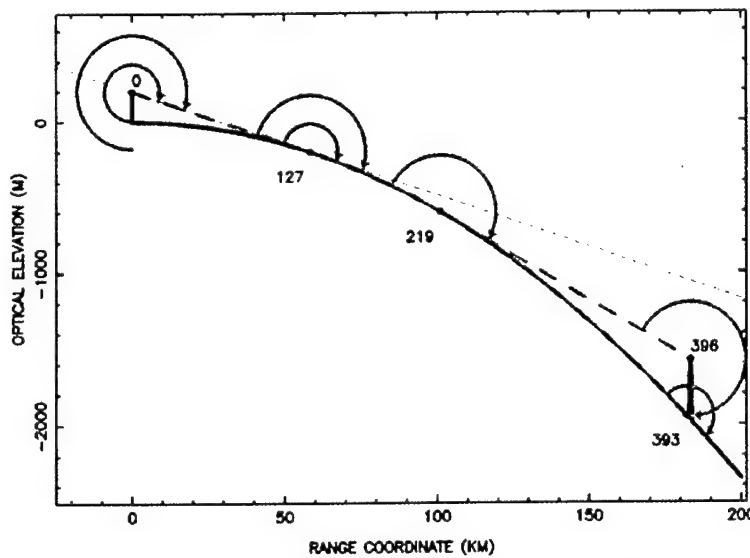


Figure 11. Knife Edge Beyond Horizon

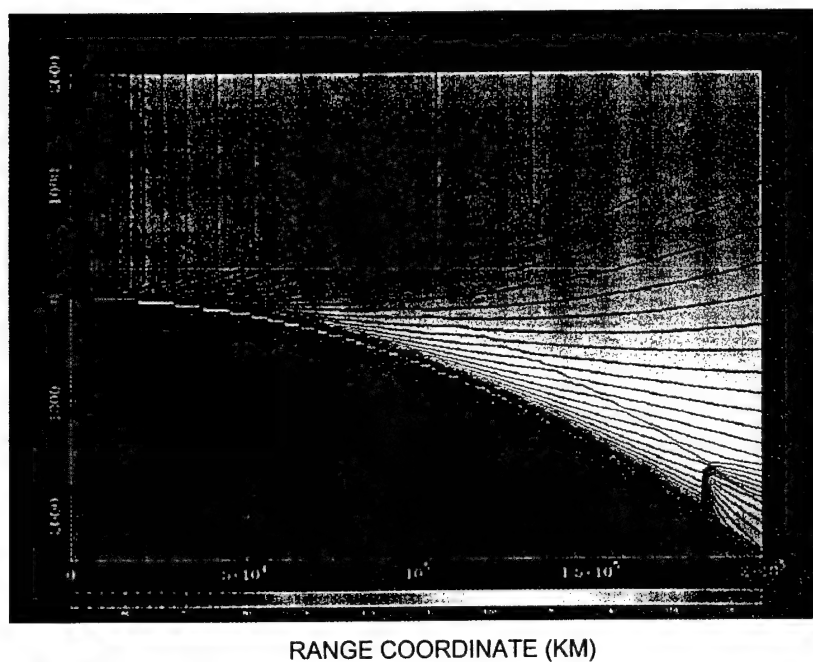


Figure 12. TMEM Knife Edge Beyond Horizon at 20.08 MHz

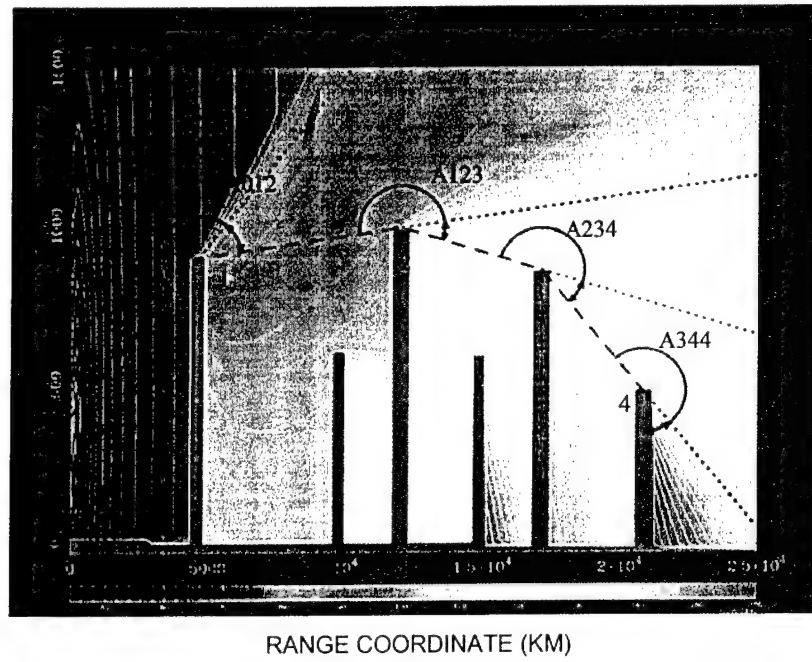


Figure 13. Diffraction Centers for Sample Terrain Profile

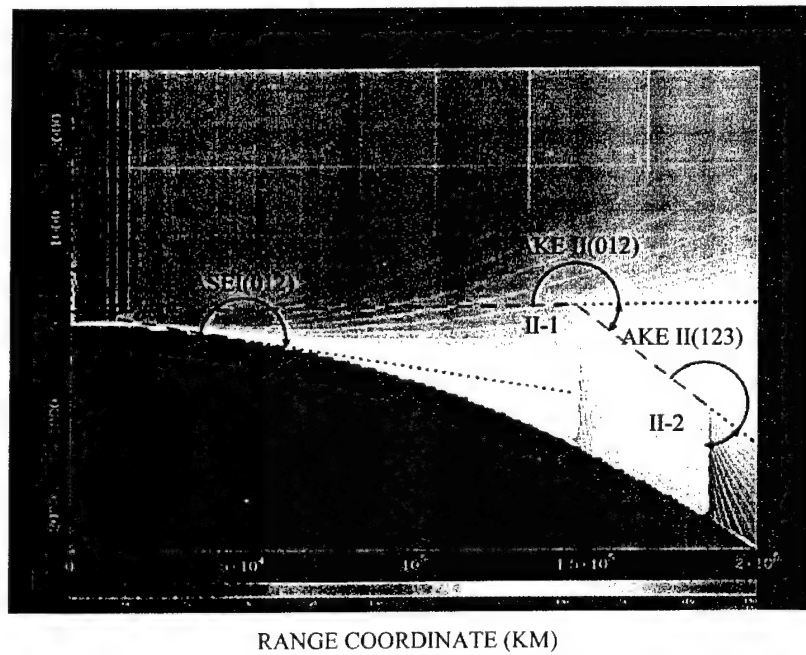


Figure 14. Smooth Earth Tangency with Visible Discrete Diffraction Center

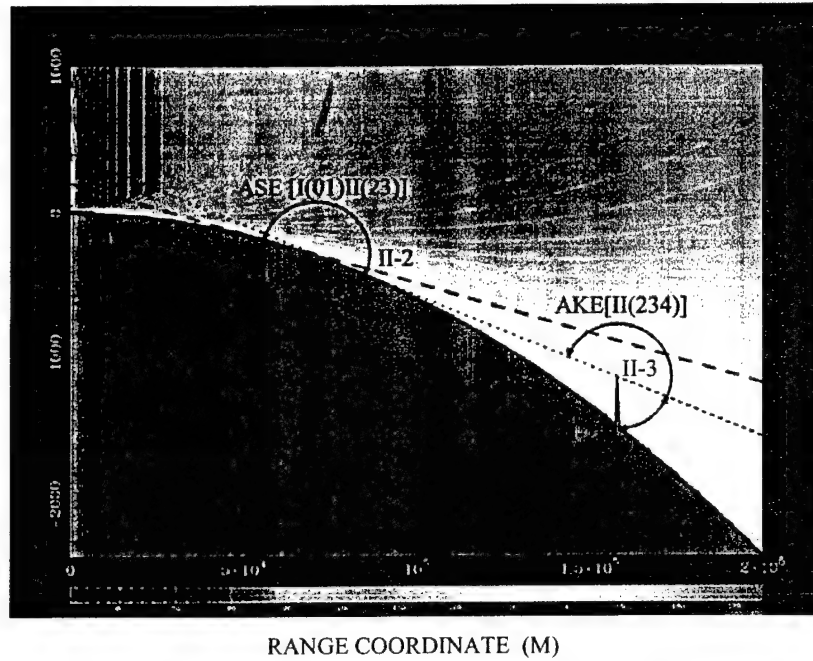


Figure 15. Knife Edge Beyond Smooth Earth Horizon

3.5. Ray Path Construction and Total Loss Calculation for Arbitrary Field Point

With the geodesic seams of the terrain profile established as the essential intermediates for ray path construction, it becomes possible to establish the geodesic path and therefore the discrete and continuous diffraction centers of relevance to an arbitrary field point. As in the analysis associated with geodesic path extension, the geodesic path to an arbitrary field point may be regarded as the composite of the geodesic path to the critically convex terrain point, defined below, and the ray path from that point to the field point. Referring again to the notation and geometry of Figure 16, the convex critical point is the terrain point (I_1) of largest range with most immediate lesser relation (I_0) of the geodesic path which admits to a negative curvature in the approach to the field point (I_2). Associated with the convex critical vertex is a radial sector bounded above by the extension of the geodesic path approaching the vertex and bounded below by extension of the path to the next geodesic point of the path. As shown in Figure 18 the sectors may be further subdivided by intermediate obstructions if the defining knife edge also serves as a branch to lesser order geodesic paths interior to the outer-most geodesic path. In the following section the more general aspects of shadow boundary continuity associated with traversal of various diffraction sectors including sub geodesic obstructions will be examined from a more comprehensive perspective.

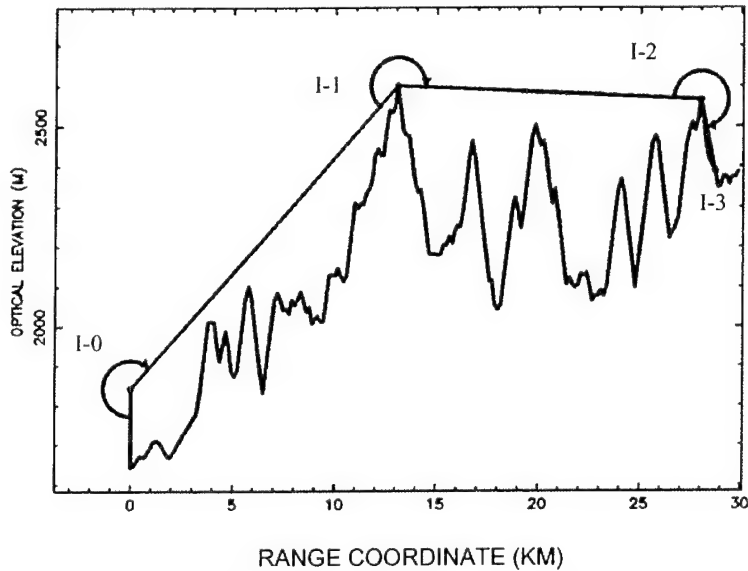


Figure 16. Geodesic Path Extension

3.5.1. Continuity of attenuation across shadow boundaries

Provided the geometry of diffraction centers, associated upper bound shadow boundaries and range dependent lower bound restriction of any sub geodesic obstructions, this section will examine the rationale for enforcement of total attenuation continuity as the diffraction sectors are traversed and the total loss is accumulated. Before considering the more general terrain geometry in which a dominant geodesic path is obstructed by a number of sub geodesic features, the basics of shadow boundary continuity enforcement may be described as applied for the simple truncated wedge appearing in Figure 17. Each of the two diffraction centers which include the vertex at the apex of the wedge and the vertex to the right of the apex is characterized by one of two mutually adjacent diffraction sectors. The upper bound of the apical diffraction sector is its shadow boundary which appears in the figure as a ray path extended beyond the vertex with the same slope as the approach to the vertex from the transmitter. The lower bound of the apical diffraction sector is the radial extension of the path from the vertex to the next diffraction center. As described below, a diffraction ray path and the associated partial diffraction loss will be computed for any unobstructed field point within the respective diffraction sector.

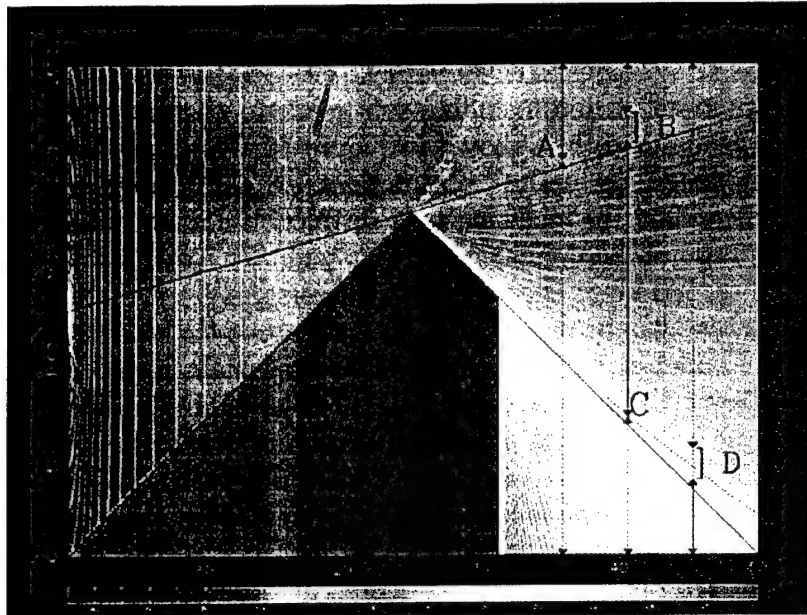


Figure 17. Shadow Boundary Continuity for Truncated Wedge

Along the vertical line passing through point A, the smooth earth attenuation is evaluated from the upper margin to the intersection with the dashed curved contour passing through point A corresponding to its value at the first knife edge and is assigned this constant value below this contour.(The assignment of the upper attenuation limit above the shadow boundary assures continuity with the loss as computed below the shadow boundary as modeled by Epstein and Peterson [1] who express the total loss as the sum of two independent single knife edge losses including that due to the first knife edge with the second knife edge as its effective field point and that due to the second knife edge with the first knife edge serving as its effective source.)

Along the vertical line containing points B and C, the first knife edge attenuation is assigned the value of 1 (zero loss) above transition region B where the scaled clearance argument reaches a value of -.78 The knife edge attenuation is evaluated by the associated knife edge attenuation function based on a 1D Fresnel integral between transition region B and point C where it reaches its maximum attenuation value corresponding to the dashed curved contour and is assigned this constant value below point C. Along the vertical line passing through transition region D, the second knife edge attenuation is assigned a value of 1 above transition region D where the scaled clearance argument attains a value of -.78 and is assigned the value of the associated knife attenuation function based on a 1D Fresnel integral value below transition region D. A more general diffraction center obstructed by sub-geodesic terrain obstacles is considered in the following section.

3.5.2. Discussion of Generalities Introduced by Sub Geodesic Obstructions (profiles with shadows obstructions)

The more general terrain profile including sub geodesic obstructions of a lower order than the external geodesic path is shown in Figure 18. Apparent in the figure are the complications introduced by optical obstructions of a diffracted ray path and the geometrical considerations for inclusion of a diffraction component from a diffraction center not among those of the dominant geodesic path. In particular, the diffracted rays attributable to the second knife edge (KE2) as illuminated by the transmitter, point (0), encounter range-dependent obstructions (KE(3-4)) between the second knife edge and the dominant geodesic outlet at KE5. The existence of an unobstructed ray path to a field point between KE2 and KE5 can be confirmed only by establishing, for each of the three subintervals imposed by the intervening knife edges that the field point in question lies above the local shadow boundary shown as a solid line in each subinterval. Beyond KE5 the knife edge labeled KE2 is no longer among the points in the dominant geodesic path extending directly from the transmitter to KE5. The partial diffraction loss due to this secondary diffraction center may be described as a function of elevation in a descent along the vertical line appearing in the figure between knife edge KE5 and the right margin. Between the upper margin and transition region T (shown as a square bracket above the shadow boundary), the partial diffraction loss due to (KE2) is the standard single knife edge loss involving source at point (0), diffraction center at point (KE2) and limiting field point at point (KE5) for which the notation AKE (025) is used in the figure. The limiting attenuation due to this diffraction center is defined by its value at KE5. Below the transition region, the partial diffraction loss due to the second knife edge beyond KE5 is assigned the constant value given by this upper bound attenuation. The similarity of this modeling to that used for diffraction centers within the dominant geodesic path assures a continuous transition to geometries in which the considered obstruction would be among the dominant diffraction centers.

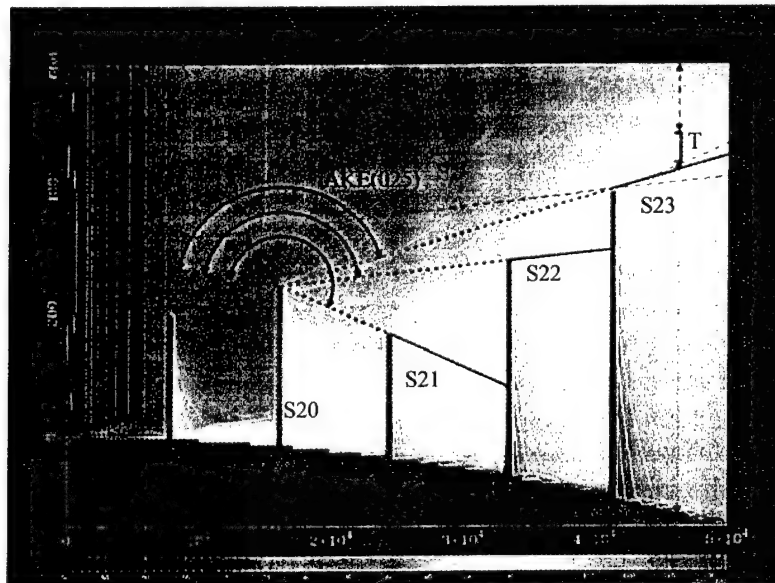


Figure 18. Sub Geodesic Diffraction

3.6. Fused wedges

In anticipation of the comprehensive desirability of a propagation model which is at once capable of treating terrain including both irregular and artificial features with piecewise linear faces as in polygonal obstacles, it becomes necessary to include a terrain geometry recognition feature which detects portions of piecewise linear terrain including those features essential in the processing of the diffraction centers. A representative profile including both irregular terrain and a block shaped obstacle intended to suggest a schematic representation of a building appears in Figure 19.

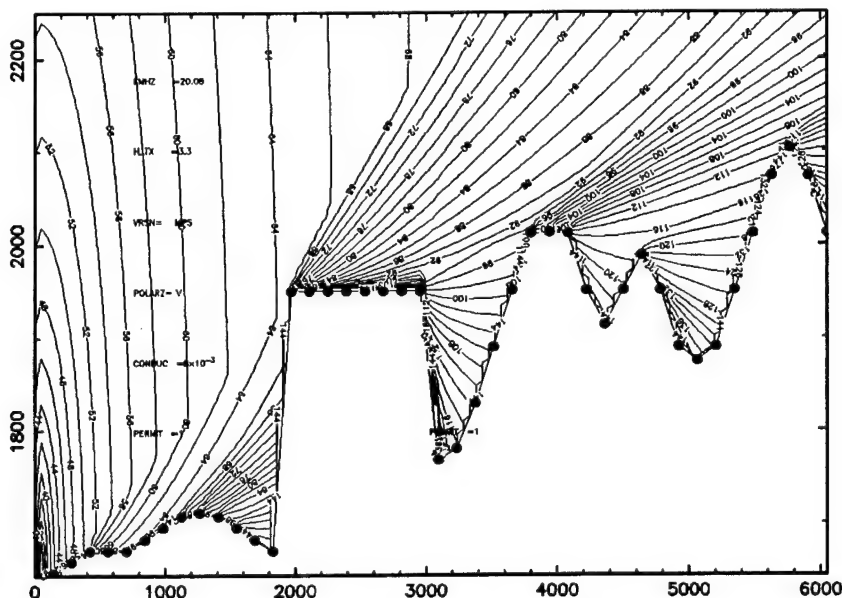


Figure 19. Terrain Profile with Polygonalizable and Irregular Terrain

Since the defining feature of the artificial obstacles is the presence of any piecewise geometrically linear faces which can only be represented with discrete profile assignments by collinear points, the algorithm described earlier for identifying geodesic seams imbedded in the terrain profile was enhanced to include a local co-linear detection feature which in its examination of terrain points simultaneously inspects for co-linearity involving each point in the profile and the corresponding two previous contiguous points. Upon detecting any isolated three such co-linear points, a line segment is initiated and possibly extended by any subsequent points conforming to the co-linearity criterion. The relevant line segment is extended until a non linear terminus is detected and the continuous set of points comprising a co-linear segment is provided an identifying segment index and the constituent points are each labeled as components of the segment. Anticipating the use of single and multiple wedge diffraction according to the methods of the uniform geometrical theory of diffraction (UTD) to model the diffraction associated with the vertices defined by adjacent co-linear segments, the dependence of UTD upon only the internal wedge angle defined by adjacent co-linear segments permits the elimination of the interstitial points of the detected line segments in which only the endpoints are retained. Since any two adjacent co-linear segments will have a common

point, the composite construction consisting of the two adjacent line segments and their common point vertex is sufficient to define a UTD diffraction center provided the geodesic path to the diffraction center is also provided. As an example, the profile appearing in Figure 19 is observed to contain a continuous sequence of co-linear points defining the upper face of a rectangular obstacle and elimination of the associated interstitial points produces the (co-linearly) reduced profile appearing in Figure 20.

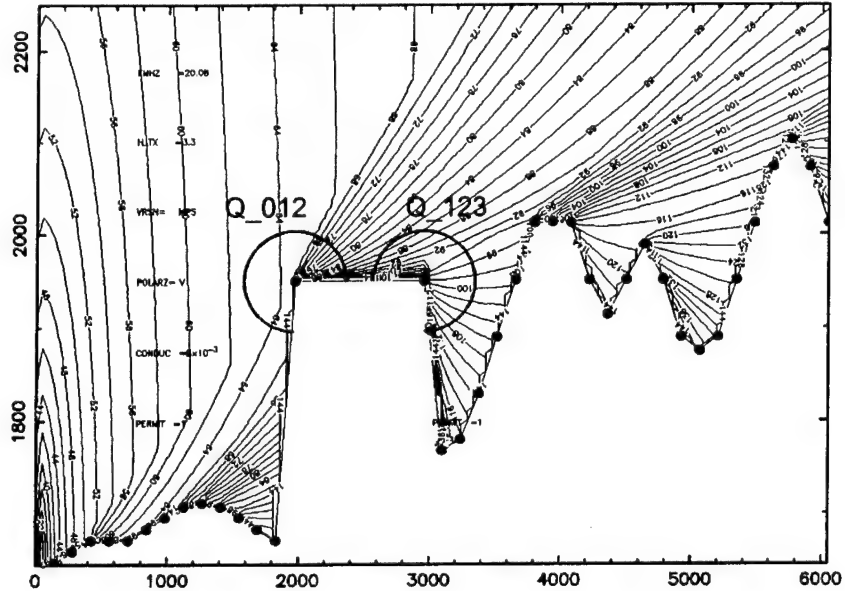


Figure 20. Terrain Profile with Polygonalizable and Irregular Terrain After Removal of Interstitial colinearities (Reduced Terrain)

Since the endpoints of the artificial terrain feature are also diffraction centers, the two complementary faces for completing the geometry of the two (fused) wedges are both taken as their most immediate non collinear relations. Thus the co-linearly reduced profile appearing in Figure 20 includes the two diffraction centers labeled in the figure and the critical internal wedge angles required for wedge diffraction are defined as the angles spanned in a rotation about the diffraction centers between the corresponding bounding collinear faces. In Figure 20 the two diffraction centers labeled Q_{012} and Q_{123} are then characterized by the internal wedge angle complementary to the arc centered at the labeled point and extending between its most immediate (reduced) terrain relations. The identification of diffraction centers defined by two co-linear segments is accomplished by assigning a value of one to a UTD identification flag which is assigned for all diffraction centers and otherwise initialized as zero. Any subsequent calculation of diffraction related quantities involving such diffraction centers will be executed according to the relevant UTD formalism including single and multiple serialized and fused wedge composite structures. The following section will describe utilization of knowledge of the geodesic paths to alls diffraction centers and their forward propagation direction optical obstructions to extract the relevant arguments for UTD diffraction.

Since the geodesic paths and forward propagation optical shadows are available for all diffraction centers including those with positive UTD identification flags and since geodesic illumination is assumed for all relevant diffraction calculations, the standard source coordinates ρ' and ϕ' are the polar coordinates of the source point associated with the most immediate geodesic relation in the direction of the transmitter. These source coordinates are computed in a coordinate system with the diffraction center as origin and with rotated Cartesian axes defined by the unit vector e_1 in the direction of the most immediate terrain relation in the direction of the source and therefore aligned along the illuminated side of the wedge, and an associated orthogonal unit vector defined by $(\hat{e}_1) \times (\hat{k})$. The field point coordinates, ρ and ϕ , are the radial coordinates of the relevant receiver target as computed in the same coordinate system. The processing of the diffraction centers designated as compatible with the methods of UTD is expected to proceed identically to those modeled as elements of serialized knife edge or smooth earth diffraction centers including establishment of immediate local source relations and evaluation of upper bound attenuations at any optical obstructions in the direction of forward propagation. The specific complex partial UTD field component contributed to a sequence of serialized diffractions is given by the relation

$$E_0^i = E_0^{i-1} D(\rho', \phi', \rho, \phi) \left(\frac{(s_t - s)}{s_t s} \right) e^{-iks}$$

where E_0^{i-1} is the complex incident field as propagated along the relevant geodesic path to the diffraction center in question, D is the UTD diffraction coefficient of Kouyoumjian and Pathak and where the final factor is the spreading factor constructed from quantities s_t and s which are, respectively, the sum of all finite ray path elements encountered in the geodesic ray path to the diffraction center, and the final ray path component from the diffraction center to the field point.

In the interest of enhanced conformity with earlier methods involving diffraction simulation with perfectly absorbing knife edges, it has been found possible to use this defining basic element in conjunction with image theory to closely approximate the loss patterns of wedge diffraction. Considering the evaluation of the field point labeled R in Figure 21, the knife edge attenuated fields are independently evaluated at the field point r , to obtain $E^{KE}(r)$, and at the virtual image r' to obtain $E^{KE}(r')$. The virtual receiver vector r' is obtained as the reflected image of r through the dark surface of the wedge (with normal unit vector \hat{e}_2 as shown in Figure 21 according to the reflection operation:

$$r' = r - 2(r \cdot \hat{e}_2)\hat{e}_2$$

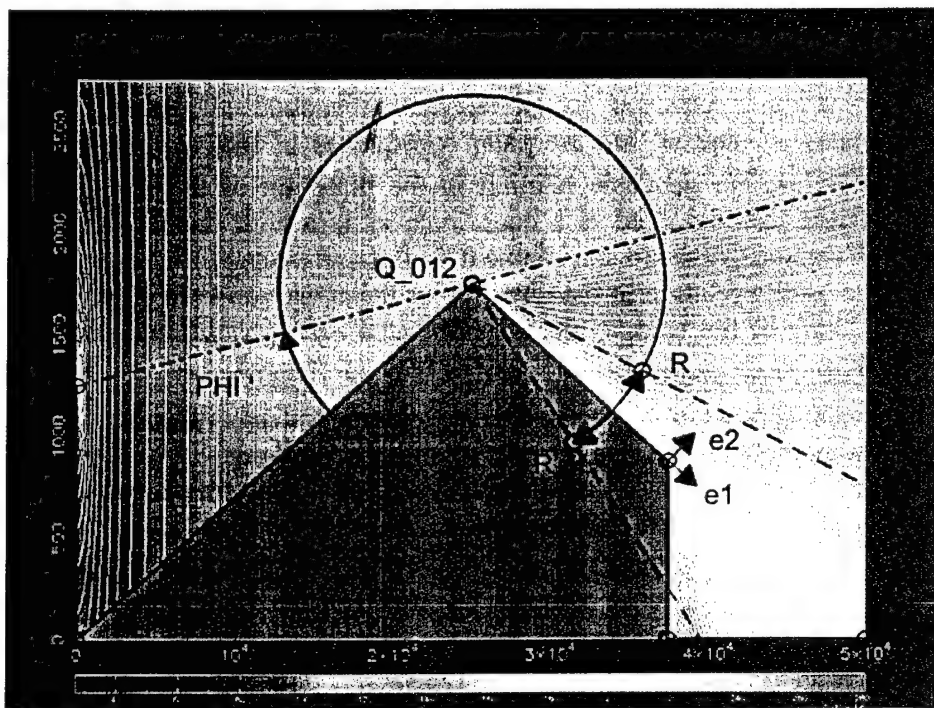


Figure 21. Use of Image Theory to Simulate Wedge Diffraction with Fresnel (Half Plane) Diffraction Theory

A reflection coefficient for this process is then evaluated consistent with a field points inclined relative to the reflecting surface with skew angle $\psi = w_x - \phi$. A similar pair of partial fields is then constructed as before using the image of the transmitter, obtained as a reflection through the lit face of the wedge which also requires evaluation of the relevant reflection coefficient with an inclination from the reflecting surface of skew angle $\psi = \phi$. The four conjugate partial fields are then superposed to obtain the total diffracted field as

$$E = E^{KE}(r_{TX}, r_{RX}) + R_n E^{KE}(r_{TX}, r'_{RX}) + R_0 (E^{KE}(r'_T, r_{RX}) + R_n E^{KE}(r'_T, r'_{RX}))$$

The agreement with the exact UTD results as shown in the vertical excursion plots of Figure 22 and the contour plots of Figure 23 and Figure 24 is encouraging.

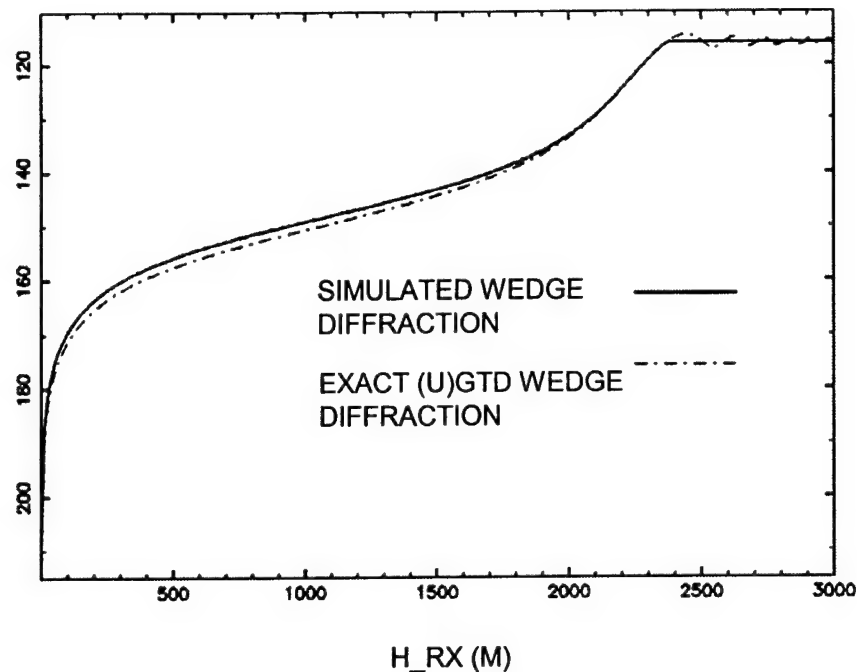
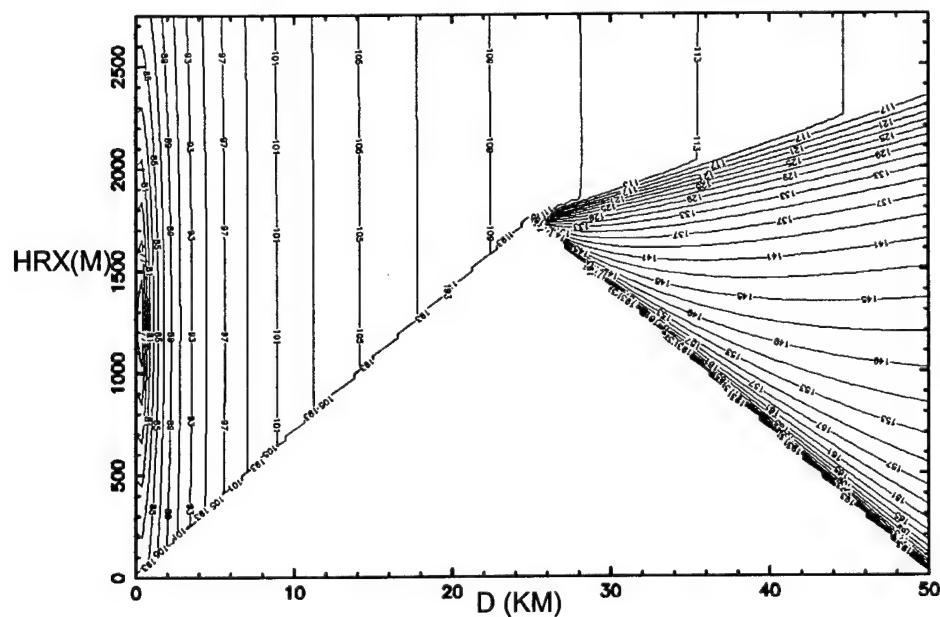


Figure 22. Knifed Edge Simulated Wedge Diffraction



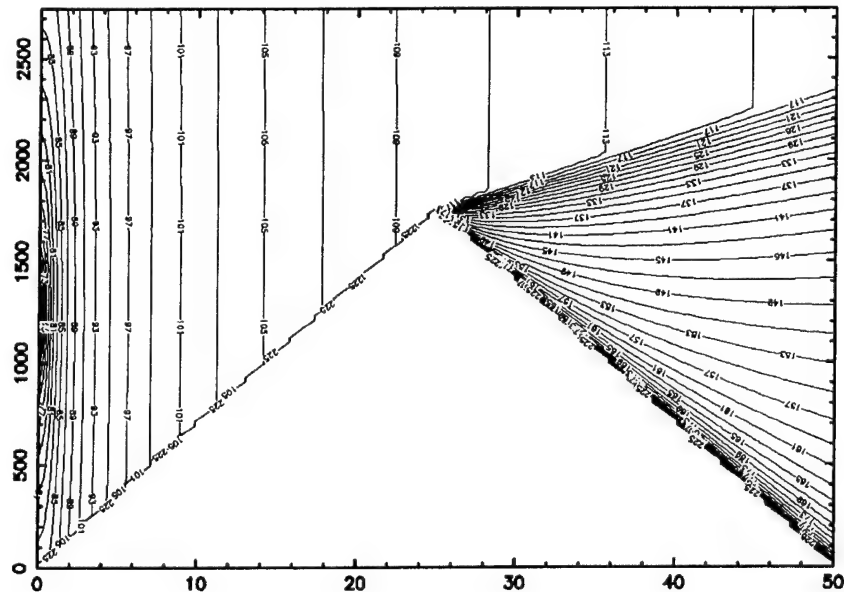


Figure 24. Propagation Plane Path Loss Contours for Wedge Diffraction Obtained Using Exact (U)GTD

4. Results

The latest trial test for the TMEM propagation algorithm show promising results. This section compares TMEM to other existing propagation models in several different test cases.

The first test case seeks to isolate diffraction from the other phenomena. In this case a transmitter at 1,278 meters MSL, vertical polarization, min range = 25 km, max range = 50 km, min height = 1,248 meters, max height = 3,248 meters for AGL and MSL, number of ranges = 201, number of heights = 101, the terrain profile in range and height in meters to (0, 0), (25, 1, 748), and (50, 0).

The PE methods demonstrate the underlying physics very well. TMEM and TIREM match the PE methods quite well in the shadow region.

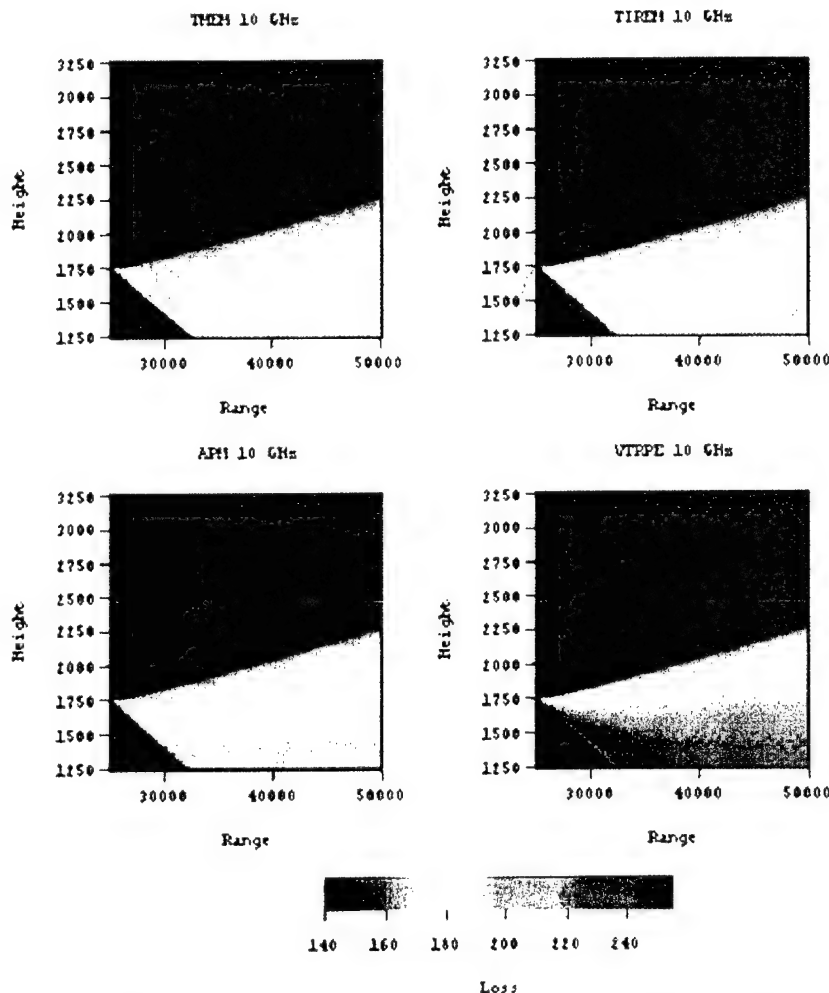


Figure 25. Wedge, Model Comparisons at 10 GHz, Vertical Polarization

The next test case involves an 80 km terrain segment of North Table Mountain, obtained from the Institute for Telecommunication Science. In this case a transmitter at 5 meters AGL, vertical polarization, min range = 0 km, max range = 80 km, min height = 1,450 meters, max height = 2,200 meters for AGL and MSL, number of ranges = 301, number of heights = 401.

The PE method demonstrates the underlying physics very well. TIREM and TMEM match the PE methods quite well in the shadow region.

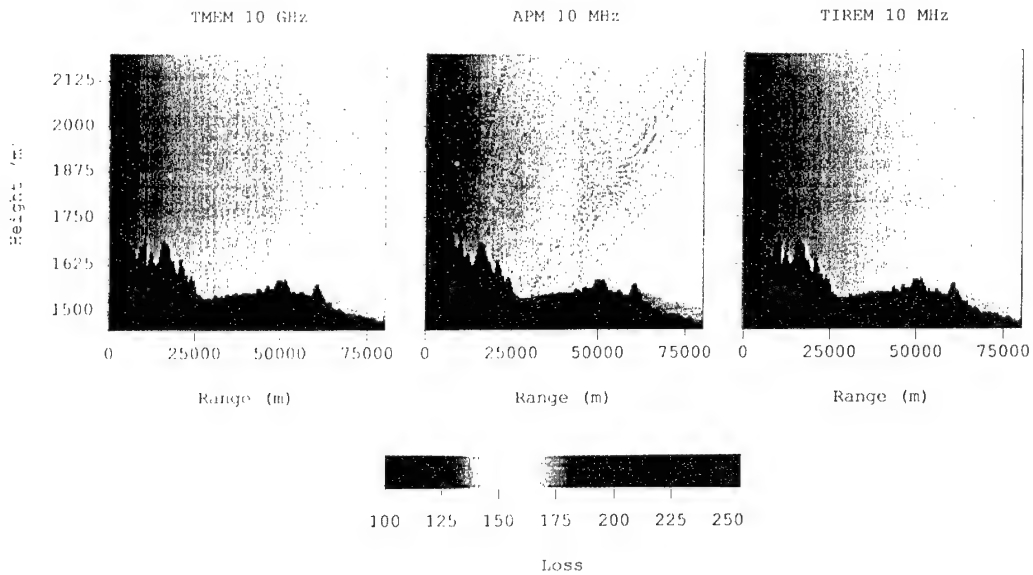


Figure 26. ITS Terrain Data, Model Comparisons at 10 GHz, Vertical Polarization

The last test case involves a 50 km terrain segment of the Colorado Mountains. In this case a transmitter at 7 meters AGL, vertical polarization, min range = 0 km, max range = 50 km, min height = 1,600 meters, max height = 3,500 meters for AGL and MSL, number of ranges = 251, number of heights = 301.

The PE method demonstrates the underlying physics very well. TMEM and TIREM match the PE method quite well in the shadow region.

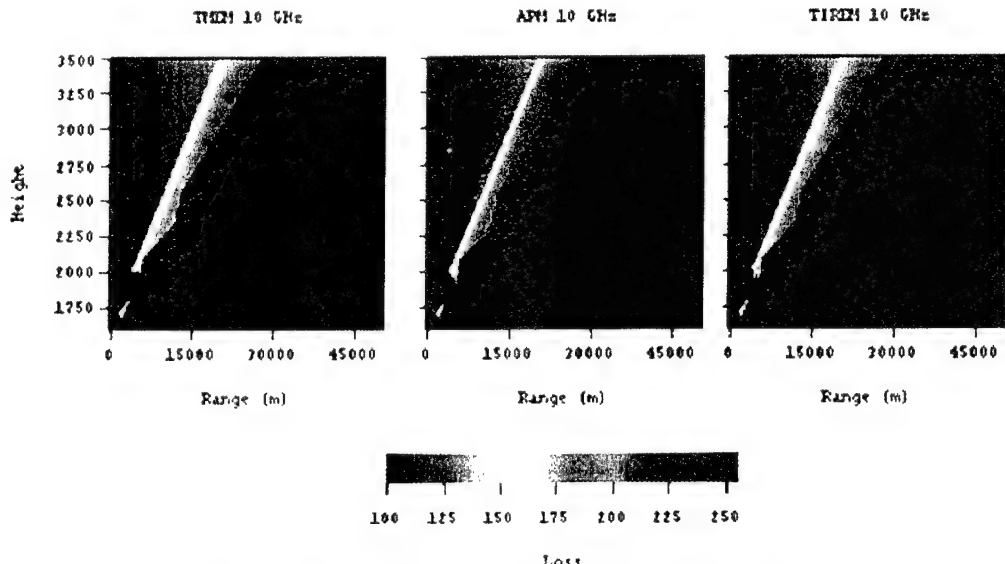


Figure 27. Colorado Mountains, 50 km Range, Model Comparisons at 10 GHz, Vertical Polarization

5. Further Research

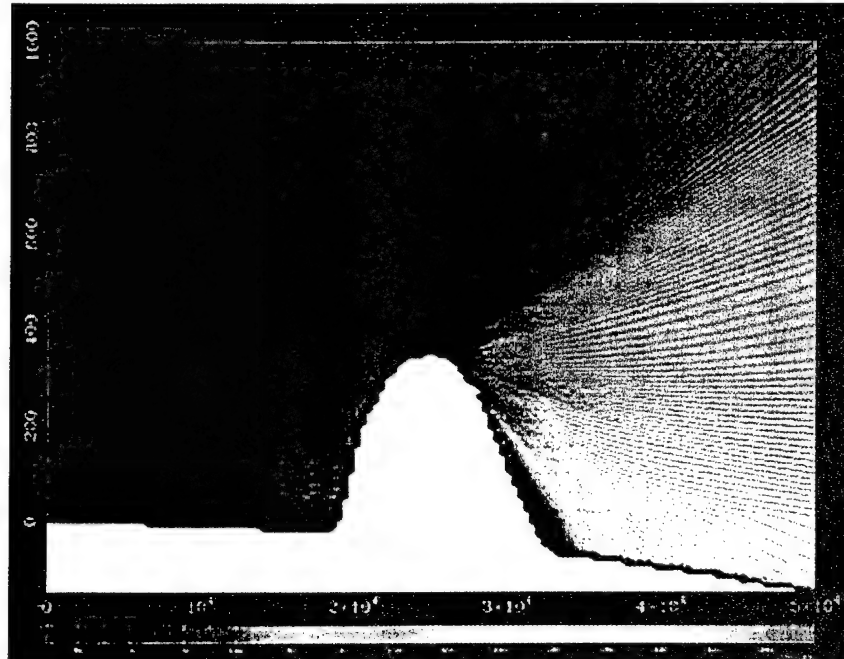
Additional research planned for the Terrain Multipath Electromagnetic Model is detailed in the following sections.

5.1. Adjustment of Excessive Loss for Multiple Knife Edge Attenuations and for Overlapping Shadow Boundaries

The essential equation for computing attenuation as modeled by a perfectly absorbing knife edge is derived from asymptotic properties of the more rigorous formulations which result from the assumption that displacements in range are much greater than the orthogonal displacements in elevation. The exaggerated excess losses observed earlier for the proposed model in comparison with TIREM, displayed again in Figure 28, are an illustration of a violation of those basic assumptions in that the separation of knife edges is only 200 meters. Although somewhat arbitrary lower limits could be imposed on knife edge spacing , its is the intention of this effort to include attenuation compensation factors which will properly adjust the excessive multiple diffraction resulting from diffraction centers of less than optimum spacing. Deygout [88] has derived an expression which serves as a double knife edge attenuation correction which could be applied for each of the successive knife edges pairings defining a multiple knife edge configuration and is of the specific form

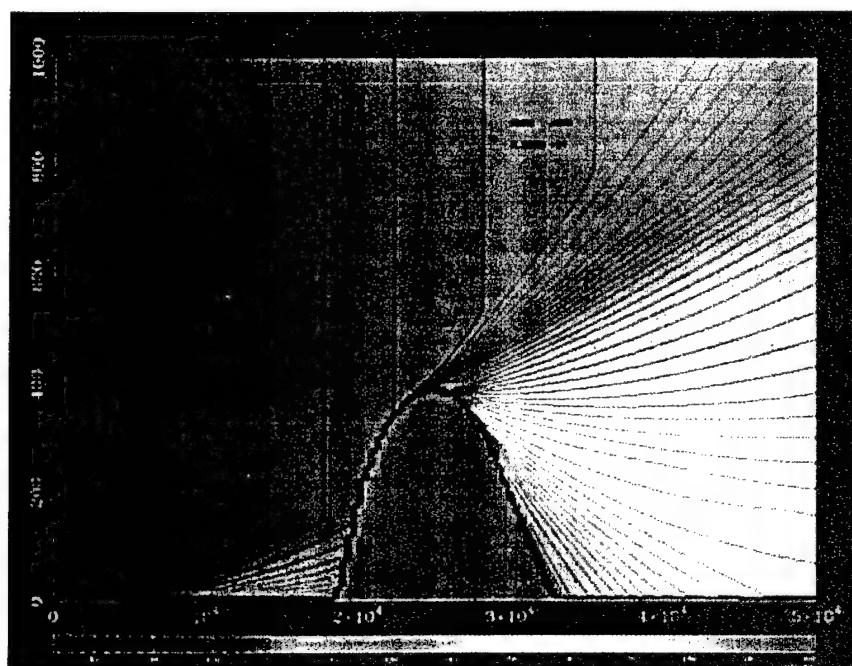
$$\beta_{cor} = 2 \left(1 - \frac{\alpha}{\pi}\right) \left(\frac{q}{p}\right)^{2p}$$

where q and p are scaled knife edge heights and α is the geometrical adjacency parameter derived in the exact two knife edge study of Millington et. al. [9]. If the spacing parameter is ideal, α assumes the value of $\pi/2$, and the knife edge correction factor is 1 but as alpha approaches a vanishing value, the correction attenuation factor approaches 2 for a loss correction that results in 6dB less loss, provided both knife edges lie along the line between antennas for which the initial calculation would otherwise yields a loss associated with two attenuation factors of (1/2) or $loss = -20\log_{10}[(1/2)(1/2)] = 12dB$.



RANGE COORDINATE (M)

Figure 28.



RANGE COORDINATE (M)

Figure 29.

The multiplicity of knife edge for this particular simulated profile is also somewhat due to the choice to model a structure with artificial polygonal segments with exact linear height functions as a function of the range. Since the coordinates understood to be elevations above sea level necessarily exclude earth curvature, the construction of the actual optical obstructions essentially transforms the linearly modeled terrain segment with zero curvature into convex curves with a negative curvature equivalent to that of the $4/3$ earth. The curvature detection algorithm described earlier correctly detects the corresponding portions of terrain with continuous negative curvature and the associated terrain points are processed as knife edges. Since the terrain profiles are elevations above sea level, optically linear constructions of zero curvature can only be constructed by including a compensating positive curvature directly into the terrain profile. If the terrain spacing is increased by a factor of two to the more typical spacing approaching 15 seconds and if the terrain profile is adjusted as suggested here to model surfaces of zero curvature in the optical environment of a $4/3$ earth atmosphere, the plot appearing in Figure 29 results. The less lossy nature of the resulting propagation modeling is readily apparent from the spacing of contour lines which is 2dB in both Figure 28 and Figure 29. In view of its effectiveness in the reproduction of exact results for two knife edges covering a wide range of knife edge proportions, it is realistic to expect the gain factor of Deygout to critically assist in providing results similar to that of Figure 29 without the uncertainties of artificial terrain or knife edge spacing restrictions. For truly linear terrain obstacles as intended in this particular test profile, modeling by perfectly absorbing knife edges is less realistic and it becomes necessary to introduce the methods of GTD, discussed in the following section, to properly model the associated diffraction.

The juxtaposition of linearly uniform segments defines a diffraction center characterized by an interior wedge angle, a geodesic orientation with respect to an effective transmitter source and therefore admits to a modeling consistent with the wedge diffraction formalism of Koyoumjian and Pathak [6]. A multiplicity of such constructs justifies the standard serialization of multiple wedge diffraction centers inherent in the methods GTD in which effective serialized source geometries are defined and caustic flux preserving spreading factors are well established. The existence of terrain realistic impedance boundary conditions, serialized geometries which introduce overlapping shadow boundaries and the presence of horizontal polarization especially in association with metallic surfaces requires a supplementing of GTD with slope diffraction and its semi-heuristic adaptations to finite ground constants [3], [4], [7]. The desirability of GTD was discussed in an earlier related progress report including coverage plots of loss in the vertical propagation plane for a truncated wedge Figure 17 and for the rounded wedge appearing in Figure 28 and Figure 29. The functional dependence of the associated GTD formalisms on source coordinates (ray path magnitude and angle of approach) and corresponding field point coordinates eliminates the uncertainties of knife edge spacing tolerance for such obstacles exhibiting the requisite polygonal geometry. Results for the same calculation at 300 MHz (high conductivity; horizontal polarization) with full access to the methods of GTD and slope diffraction available to the TMEM GTD Addendum appear in the upper left panel Figure 30 (and for 5000 MHz and in Figure 31). The accompanying panels of Figure 30 display results for the same problem but using alternate propagation models, TIREM, APM and parabolic equations (VTRPE). The TMEM GTD addendum appears to provide an adequate approximation of the

numerically exact results shown in VTRPE. Since the underlying optical geometrical parameters for computational GTD as dictated by inter-relational geodesic geometry are direct generalizations of those required for the basic diffraction elements presently implemented in the developing proposed model, the extension to GTD and higher order adaptations is expected to be a minimally invasive enhancement of current methods, fully implemented within the established computational infrastructure.

Finally the existence of inhomogeneous earth ground constants as most conspicuously exemplified by transitions between land and sea will require an additional flexibility to appropriately adjust ground constants and weighted partial paths loss contributions to be in conformity with established limiting quantitative characteristics of path loss for propagation over mixed land and sea paths.

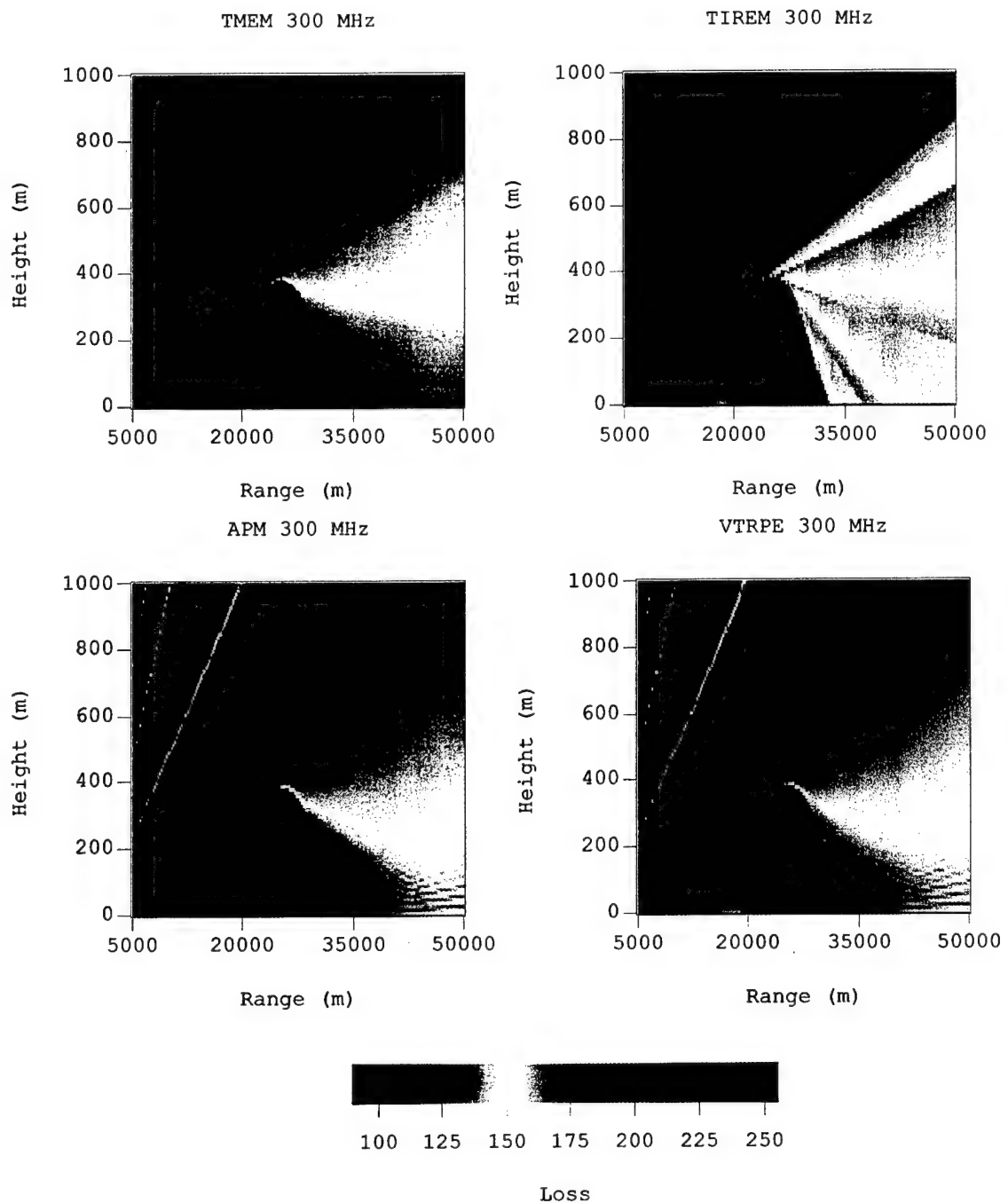


Figure 30. 300 MHz

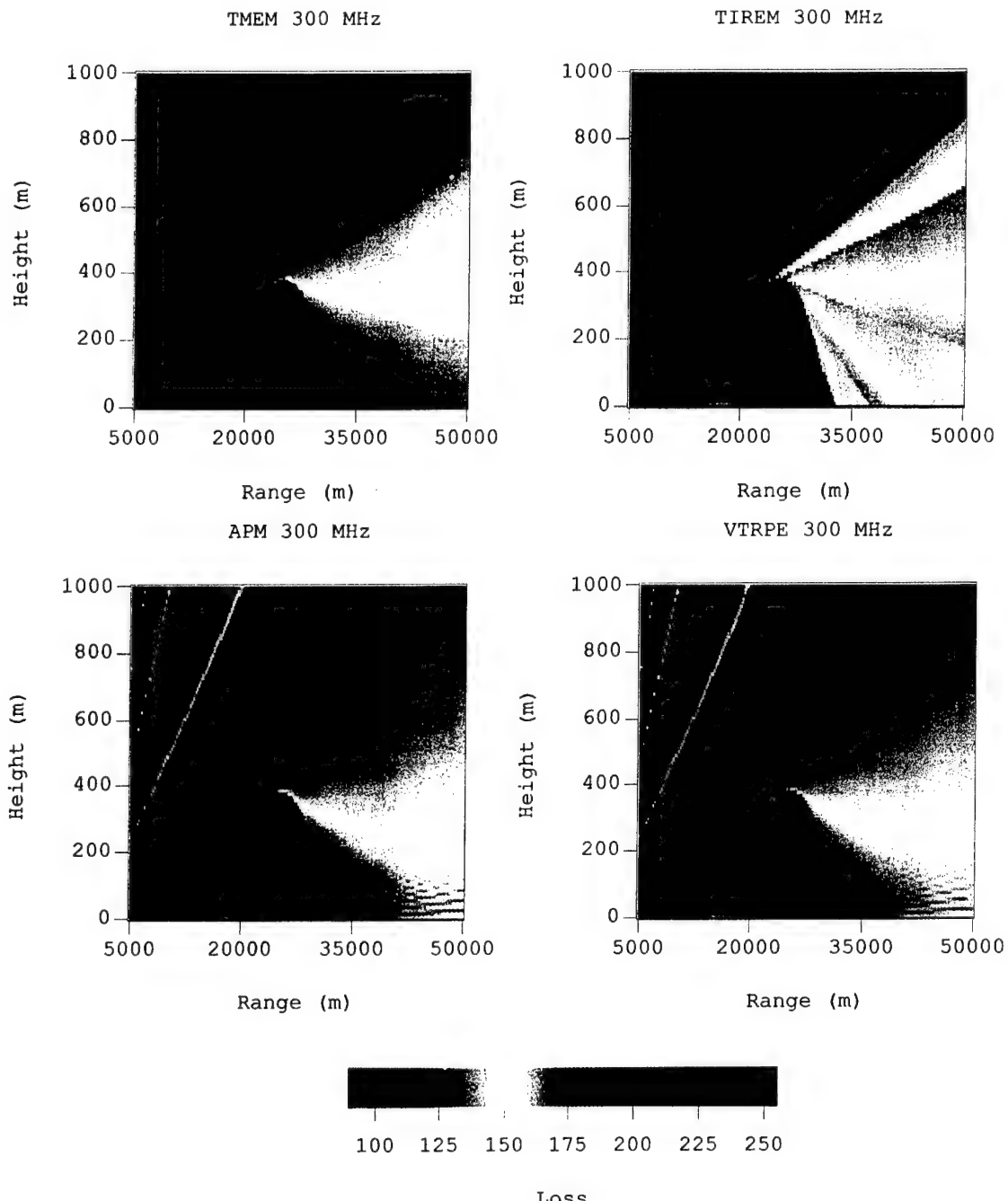
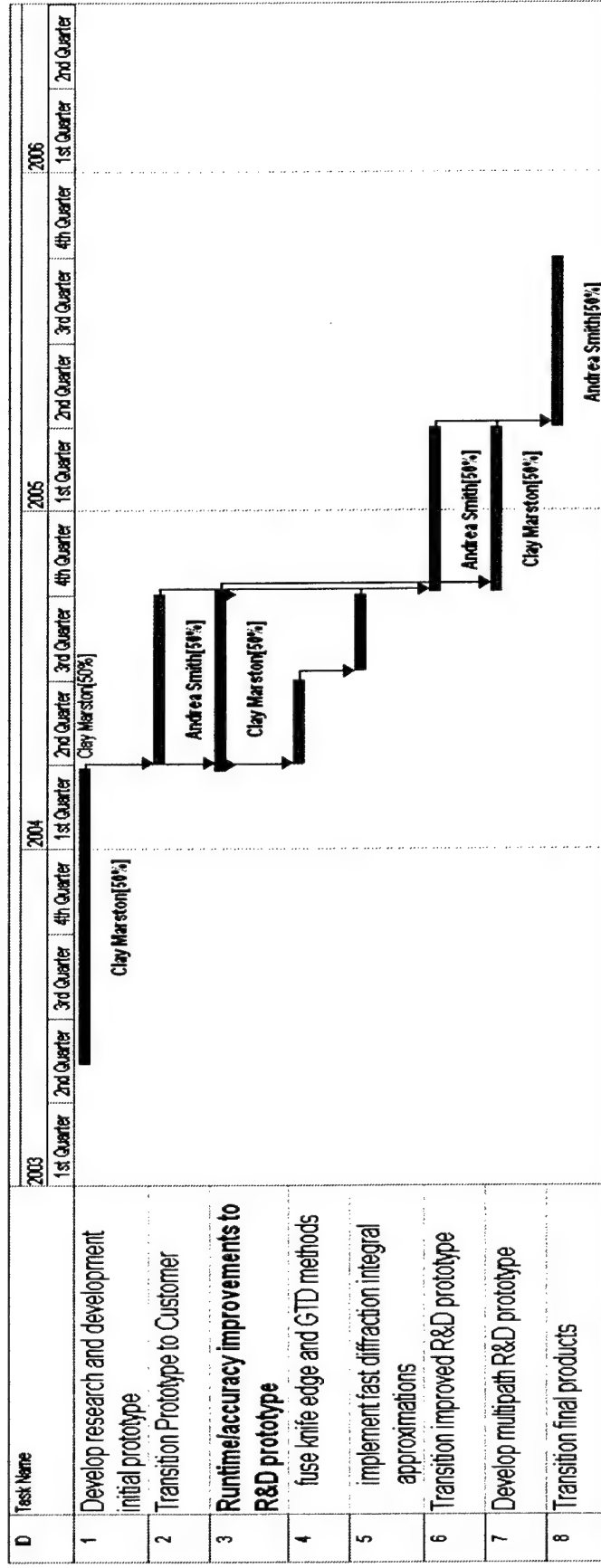


Figure 31. 5 GHz

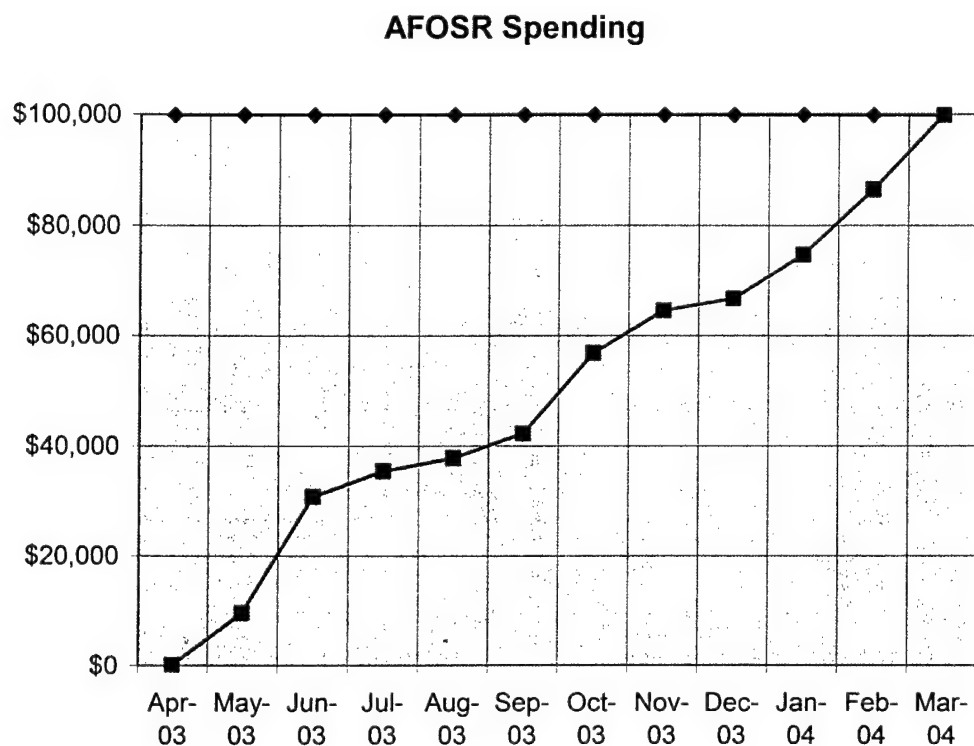
5.2. Performance Enhancements

This phase of research and development has focused on the development of a physically accurate propagation model. As the model is slated for use in a real-time system, it must run as such. Thus, significant improvements to the speed and efficiency of the algorithm are planned.

6. Schedule



7. Spending Record



8. Personnel Support

The Principle Investigator for this project is Dr. Stephen A. Fast. Serving as Research Scientist leading the Government Service Division of Remcom Inc. is Stephen A. Fast. Dr. Fast, who holds a Ph.D. in mathematics, has previously occupied Research Associate positions at the Applied Research Laboratory at The Pennsylvania State University, the Applied Research Laboratory at the University of Texas at Austin, the Atlantic Research Corporation's Electromagnetic Environmental Test Facility, and the U.S. Army Signal Corps. The work done at Remcom has thoroughly benefited from Dr. Fast's academic background and expertise. His research pursuits include: electromagnetic propagation modeling and techniques, cellular phone modeling methods, evaluation of tactical communications and intelligence systems. These intellectual enterprises have shaped a remarkably broad range of professional accomplishments at Remcom, such as the development of the Electromagnetic Propagation Integrated Resource Environment (EMPIRE), and a single point urban geolocation method based on urban propagation predictions. Dr. Stephen Fast has also led the Remcom in a highly successful collaboration with the PSU Meteorology Department, which focused on the development of atmospheric interpolation methods for anomalous conditions that may be used in support of radio wave propagation.

Supporting Dr. Fast is Dr. C. Clay Marston. Dr. Marston recently joined Remcom after serving as the primary theoretical, algorithmic, and software developer of TIREM at Alion Science and Technology Corporation. Dr. Marston holds a Ph.D. in physics and has conducted fundamental research in quantum mechanics and theoretical electromagnetics. His current research interests include numerical methods in electromagnetics especially diffraction and scattering. His work improving the methods of TIREM and other ray based propagation models have resulted in new techniques for more rigorous methods that are computationally efficient.

M. Jeff Barney is an undergraduate electrical engineering student at The Pennsylvania State University. Jeff is interested in terrestrial propagation and has investigated the various differences of many RF propagation models including VTRPE, APM, ITM, TIREM, Prophet, RPO, and MMwave. Additionally, Jeff has developed methods to derive worldwide foliage maps used to support RF propagation through foliage.

9. Publications

The results of the first portion of this work are being prepared for submission to Radio Science.

10. Interactions/Transitions

Soon after the end of the first year, the results of the first phase shall be transitioned to the JCS.

11. New discoveries, inventions, or patent disclosures

N/A

12. Honors/Awards

N/A

13. Appendix – Earlier Progress Report

13.1. Accomplishments/New Findings

13.1.1. Baseline run times and model comparisons

Prior to implementing any new methods or algorithms, existing models' performance was investigated. Several benchmarks test cases were run to compare run times and propagation predictions. Thus, those areas requiring improvement were identified. Thus far, we have explored the terrain extraction performance, compared the predictions for various models for a few standard test cases, and made performance comparisons using the most promising existing models and algorithms to apply to the JCS.

13.1.1.1. Terrain extraction study

There are several methods to compute the points along a great circle path. To extract terrain between two points, the range and bearing between them must be computed. Then along the great circle, latitudes and longitudes must be found and corresponding terrain computed from the National Imagery and Mapping Agency (NIMA) Digital Terrain Elevation Data (DTED). Below we discuss the methods that could be applied. In accordance with the JCS requirements, only 1 km DTED terrain data will be used and the maximum area over which terrain will be used in 400x400 square kilometers.

13.1.1.1.1. Modified Rainsford Method

The modified Rainsford method is one of the most accurate methods. This method utilizes a real earth model, i.e. WGS-84, and an iterative algorithm to provide very accurate calculations for the forward and inverse problems, i.e. computing a point on the earth given the range and bearing from a given point and computing range and bearing given two points on the earth. However, with respect to performance the iterative nature of the algorithm can cause unnecessary increases in time and complexity, especially when a tolerable level of error can be achieved with less complex algorithms.

13.1.1.1.1.2. Linear Interpolation

This method simply treats the latitude longitude grid as a Cartesian coordinate system with latitude representing X and longitude representing Y. Using this method the end points of a bearing act as the end points of a line between the two locations and using the parametric representation of this line we can find the location of any points in between. This method is simple and very fast; however it can produce large errors as distance from the equator increases.

13.1.1.1.1.3. Great Circle

This method uses a perfect sphere to represent the surface of the earth. This is a more reasonable approximation than the flat earth model used in the Linear Interpolation method, but is not as accurate as the real earth model used in the modified Rainsford method. Using this method is a compromise between the two previous methods providing more accuracy with a slight performance penalty. This method primarily uses trigonometric functions.

13.1.1.4. Test Results

To determine the potential run time improvement over the Modified Rainsford Method of the other methods, a test was run in Nellis AFB and surrounding area. The test was designed to approximate operation in a 400 km X 400 km area. For simplicity we chose a slightly larger area that spanned 4 degrees X 4 degrees. This area was sampled on the diagonal for a total of 100000 points. The results are depicted in Table 1 below.

Table 1

	MRM	GC	Linear
Max Difference in meters from Modified Rainsford Method	0 m	181.781 m	4957 m
Speed up compared to MRM	N/A	5/3	10^3

13.1.1.5. Optimization

Further optimization may be performed by allocating fewer temporary variables and precomputing certain values for the Great Circle method. Another possible solution is to combine the methods in a dynamic way such that depending on the area of the world and path length. A combination between methods may allow a better balance of performance and accuracy. Investigation of optimizations for the Modified Rainsford Method has not been completed and a closer investigation of the method may reveal some possible optimizations such as pre calculation of sin/cos tables and using them as a lookup for in subsequent queries.

13.1.1.6. Recommendations and Conclusions

Although the linear interpolation is significantly faster, the error will be almost 5 terrain points at long ranges. The great circle method would interpolate between the same terrain points and resulting in an acceptable error. Thus we have begun building our software using a hybrid method between linear interpolation the great circle method.

13.1.1.2. Validation comparisons

Although there have been many papers comparing various propagation models and algorithms, e.g. knife-edge and other diffraction methods, very few if any quantitative numerical comparisons have been done. Thus there is no hard data on which to select a propagation modeling algorithm. To assist selecting a proper method for the JCS, a few simple test cases were selected and some of the currently available propagation models were compared using these cases. Before proceeding to the comparisons, the various methods and algorithms for each propagation model are discussed below.

Table 2 gives a brief summary of the models and their capabilities.

Table 2

Model	Frequency	Ground wave	Sky wave	Atmosphere	Ground	Version	Algorithm	Comments
APM	100 MHz – 20 GHz	No	No	Ducting, absorption. dependent profiles, temperature, humidity and wind speed	Terrain diffraction and reflection. Uses range refractivity surface dependent surface dielectric constants	1.3.2	FE, PE, RO, XO	Hybrid parabolic wave equation method, troposcatter
ITM	20 MHz – 20 GHz	No	No	Uses effective radius. Uses refractivity	Terrain diffraction and reflection. Terrain irregularity used. Dielectric constants used	1.2.2		Offers the capability to generate based on reliability and confidence.
TIREM	2 MHz – 20 GHz extended to 50 GHZ with MMWAVE hybrid	Yes	No	Absorption through standard atmosphere. Uses surface refractivity and surface humidity	Terrain diffraction and reflection. Dielectrics used over land.	3.14		Zero elevations are water, knife edge diffraction, troposcatter
VTRPE	100 KHz – 100 GHz	Yes.	Uses range dependent dielectric constants	Yes. Uses sunspot Number, X-Ray flux time of day and year to define the ionosphere	Ducting and absorption. Uses range dependent refractivity profiles.	Terrain diffraction and reflection. Uses dependent dielectric constants	3.99T	Full parabolic equation

13.1.1.2.1. TIREM

The Terrain Integrated Rough Earth Model (TIREM) is a general purpose point to point model applicable from 2 MHz to 20 GHz developed by the Joint Spectrum Center (JSC). TIREM models the ground wave, terrain reflection and diffraction, and troposcatter in benign atmospheres. TIREM computes the paths between the terminal points of a radio link and applies the correct theoretical model depending on the situation. When computing rays, the effective earth's radius is required and thus TIREM uses the surface refractivity to compute the effective earth's radius. Knowing the ray paths TIREM computes, rain and foliage attenuation can be computed. TIREM is one of the most thoroughly validated models. The TIREM validation report is available from JSC, the TIREM sponsor, which outlines over 10,000 real world measurements used to validate TIREM. According to the report, the mean error in TIREM vs. measured data is less than 1 dB with standard deviation around 10 dB. Further, the TIREM developers have built TIREM to run fast.

TIREM employs a hybrid method: switching between various algorithms as the conditions merit. In regions where more than one propagation mode may be present, TIREM selects the mode with the least loss.

TIREM's algorithms are very dependent on correct terrain sampling resolution. TIREM selects the radio horizon and the diffraction and reflection point by searching the terrain points. Thus, JSC recommends that TIREM is given terrain elevation points that are *no more* the 250 meters apart. Unless prominent terrain features have been identified and included in terrain profiles, JSC recommends 3 arc second DTED be used. However, terrain reflection is only considered if the Fresnel zone intersects the terrain. The Fresnel zone is the ellipse of points such that the path difference between the direct path and any reflection path with a reflection point within the ellipse is less than $\frac{1}{2}$ a wavelength. For practical purposes, this is why TIREM results do not show the strong lobing structure. The TIREM Fresnel zone approximation for reflection points means that only the structure present below the peak of the first lobe is modeled.

For terrain diffraction, TIREM applies the Epstein-Peterson knife-edge diffraction method. Depending on the frequency and the knife-edge height and sharpness, knife-edge diffraction may underestimate the loss in the shadow region. TIREM compensates for this by using a hybrid algorithm that alleviates this problem in most cases. Thus, the error in TIREM has been reduced to only a few dB in areas in the shadow well above the terrain.

Often in deep shadow regions the troposcatter path will have less loss. TIREM uses the CCIR/ITU method to predict troposcatter loss. This empirical method gives only mean results, and, thus, troposcatter results may vary significantly depending on the area of the world and time of year. In general, TIREM's method will produce reliable answers that communication planners can use to design troposcatter links.

The most notable TIREM anomaly is found in the shadow region of a broad hill. When computing the losses for a broad hill, TIREM often identifies more than one knife-edge

on the hill. This causes odd shadowing behavior between the shadow cast by the first and second knife-edges.

13.1.1.2.2. ITM

The Institute of Telecommunication Sciences (ITS) Irregular Terrain Model (ITM) is maintained by George Hufford. ITM uses ray methods together with parametric formulations to compute the loss due to reflection, diffraction, and troposcatter. ITM is applicable between 20 MHz and 20 GHz. ITM has been widely accepted in the radio and television broadcast industry. This is due in large part to the numerous measurements taken by ITS and used to validate the model and develop broadcast statistical parameters such as reliability and confidence of a radio link.

The reference attenuation is not a smooth function of distance, but is divided into three regions. The line-of-sight region extends to the smooth-earth horizon distance. Here, the bulge of the earth does not interrupt the direct radio waves and the predicted attenuation is based on two-ray reflection theory and extrapolated diffraction theory. In the next region, the predicted attenuation is a weighted average of knife-edge and smooth earth diffraction calculations. The weighting factor is a function of frequency, terrain irregularity, and antenna heights. Far outside the radio horizon, forward troposcatter effects dominate. An adjustment is made to the reference attenuation for climate to convert the reference attenuation to an all-year median attenuation.

For the diffraction region only the transmitter and receiver's horizons are used. The loss is computed using a weighted average between no more than two knife edges and Vogler's smooth earth methods. The weighting factor is an empirically determined function of frequency, the antenna heights, and terrain parameters.

Because the diffraction rays ignore the reflected component, the deep shadow shows significantly less loss than is actually present. Further, as only the endpoints' horizons are applied, diffraction effects from more than two terrain obstacles will not be evident in ITM predictions.

13.1.1.2.3. APM

The Advance Propagation Model (APM) was developed by Amalia Barrios from SPAWAR SSC-SD. APM uses a hybrid parabolic equation (PE) method to compute the attenuation from 100 MHz to 20 GHz. APM models terrain reflection and diffraction, atmospheric ducting, and troposcatter. APM uses a flat earth (FE) ray tracing algorithm near the transmitter. When the flat earth assumption is no longer valid, APM uses a ray optics (RO) method, i.e. ray tracing over a curved earth. When the transmitter is over rough terrain, neither the FE nor RO methods are applied. When the FE and RO methods are no longer valid, APM applies the parabolic equation (PE) near the ground and an extended optics (XO) method above the PE region.

To understand the importance of APM's hybrid method, first consider how the parabolic equation method works. In PE models, the transmitter antenna pattern is converted to a field distribution along a vertical line located at the calculation origin, i.e. the transmitter or zero range. The initial field is then marched (stepped) in range using a Fourier method

and an atmospheric correction. Accordingly, APM and other PE models naturally fill a vertical plane with loss data as they compute. This means that PE models are not efficient when computing an isolated point-to-point calculation, but are excellent for computing losses for a large numbers of height points. Within each range step, the field is Fourier transformed forward, a refractivity correction applied, and transformed back to the original domain. For the Fourier method to be accurate, it must have a height grid resolution of around 0.1λ . Since the vertical extent of the field cannot go to infinity, a maximum height is determined in the algorithms, and methods are applied to eliminate effects of the upper boundary of the calculation region. The maximum calculation height is related to the vertical beamwidth that the algorithm can support; more correctly the minimum and maximum angles in which energy is allowed to propagate. Needless to say, full PE methods with wide-angle capability and small range steps are computationally expensive. Thus, APM's hybrid method allows it to reduce the run time penalties inherent to PE methods. To get further run time improvements, APM also sacrifices a wide-angle capability and some accuracy resulting from using larger range steps.

The APM propagation model's narrow angle assumption results in null data for elevation angles not within specified limits. For elevation angles larger than APM's maximum, free space loss can be substituted. However, because of possible errors caused by terrain reflection, it is difficult to compensate for null APM data for angles below the minimum elevation angle. This will be most noticeable when the transmitter is high and over rough terrain.

Using APM, shadows behind obstacles often have losses similar to those observed with knife-edge diffraction, possibly because of the angle limitation and step size selection. Thus, APM underestimates the loss in the deep shadow. APM uses a fixed step size, so, occasionally; the internal APM step will not coincide with the diffraction edge. Thus the shadow boundary in APM is different than that in models which ensure the diffraction point is identified and used.

As with all PEs, the initial field in APM is found from the transmitter's antenna pattern. Thus, unlike TIREM, the transmitter's antenna pattern cannot be applied after the calculation. Also, because of the nature of the PE algorithm, APM does not provide data to an external interface in order to allow the elevation angle dependence of the receive antenna to be considered. Thus, it is difficult to receive antenna patterns when using APM.

The APM API requires that the calling application provide the refractive data. In order to interpolate the refractive data at the PE range steps, APM assumes that the refractive data can be interpolated using corresponding indices in the profile arrays. Therefore, when using APM, the calling program is responsible for arranging the refractive profiles accordingly, so that the interpolation is physically correct. In addition to refractive profile data, APM uses the humidity and temperature to compute absorption.

APM uses the wind speed to determine the surface roughness of waves over water. The wind speed is related to the wave height and spacing, and consequently, the surface roughness. The surface roughness is then mapped to an angle dependent reflection

coefficient. Thus, APM essentially accounts for surface roughness by changing the reflection coefficient. Thus, energy is not scattered, but the effects of scatter on the forward propagated energy is considered. APM allows the wind speed to be set as a function of range. Thus, the surface roughness can be varied along a path. As well as computing the surface roughness effects over water, APM is equipped to take advantage of range dependent dielectric constants.

Lastly, one manifestation of APM's hybrid scheme is an occasional inconsistency in the results as the boundary changes from the PE to the XO regions. In unpredictable situations, a feature or structure will slightly and abruptly change direction when crossing the PE/XO boundary.

13.1.1.2.4. VTRPE

The Variable Terrain Radio Parabolic Equation (VTRPE) model is one of the most versatile and precise models available. VTRPE was developed by Frank Ryan from SPAWAR SSC-SD. VTRPE can model the ionospheric sky wave, terrain reflection and diffraction, ducting, and the ground wave.

VTRPE is a full PE, i.e. no approximations are made to the PE method and no hybrid methods are used. VTRPE uses a wide-angle propagator, i.e. energy at very large elevation angles is propagated (as compared with APM which has an upper elevation angle limit). VTRPE examines the field at each range step to determine the Fourier transform size required to correctly accomplish the computations. Further, VTRPE evaluates the fields at each range step to determine the maximum acceptable step size. By allowing the Fourier transform size and the range step to be variable, VTRPE keeps the results accurate and optimizes the model execution time. Thus, if a transmitting antenna has high elevation angle contributions, e.g. an isotropic antenna, the Fourier transform size will be large and the range step size small causing longer than potentially required run times.

As with APM, VTRPE can model the effects of range dependent atmospheres and dielectric constants. VTRPE can either call out to an external program for the refractive index data at each range step or have multiple profiles passed to it. In comparison to the atmosphere, VTRPE models the ionosphere internally. The model VTRPE uses is the FAIM-D ionosphere model for the E and F layers and the smoothly transitions to the IRI model to include the D Layer.

Antenna patterns for VTRPE are treated similarly to APM, that is, the transmit antenna pattern is applied to compute the initial field. However, since VTRPE can model the ground wave, VTRPE models the complex antenna ground interaction required to properly excite the ground wave for arbitrary antennas. Thus VTRPE requires that for antennas model the ground plane is not included in the pattern. Additionally, for non HF receive antennas, since VTRPE only offers loss and no angular distribution of the energy at the receive point.

13.1.1.2.5. Comparisons

To understand the differences between the models, some simple test cases using terrain that allows the differences to be isolated were used. The configurations for these tests are described below. In all cases the frequency chosen for the comparisons was 300 MHz with vertical polarization. APM, VTRPE, TIREM and ITM were compared.

Two wedges were chosen to better quantify the effects of a second diffraction. The first double wedge case uses two wedges with difference maximum elevations. This allows the testers to see if the shadow boundary caused by diffraction from the second wedge is properly modeled. The transmitter height is 10 meters, the min range = 5 km, max range = 50 km, min height = 1 meter, max height = 1,001 meters MSL, number of ranges = 181, number of heights = 101, and the terrain profile in range in km and height in meters is (0, 0), (6.25, 200), (12.5, 0), (25, 0), (31.25, 150), (37.5, 0), and (50, 0).

The test results for the two uneven wedges are show in Figure 25. First notice the VTRPE results. The interference pattern from the direct and reflected rays is clearly present in the illuminated region. Also, we see the diffracted and reflected ray interference in the shadow regions. Evidence of reflected energy off of the front face of the second wedge is also seen. APM does almost as nice a job as VTRPE. With APM the interference pattern in the shadow of the first wedge is noticeably bent in a non-physically justifiable way. Also, since APM uses a narrow band PE propagator, the strong lobing found before the first hill is not present. In short the parabolic equation models' results demonstrate why the PE method is widely accepted as the standard. Only high fidelity ray methods such as those used in GTD Estimation of Loss due to Terrain Interaction (GELTI) will give similar results as the PE methods. Thus we should not expect TIREM or ITM to show the same features as VTRPE and APM. First, neither TIREM nor ITM model the reflected ray (except very near the ground) and thus the lobing structure is not found in these results. The transition to the shadow boundary is significantly sharper in these models. In TIREM diffraction is applied just above the shadow boundary so the transition is more realistically gradual in its results. ITM, however, does not model this at all and the transition is very abrupt. Lastly, in the shadow of the first hill, TIREM underestimates the loss.

The second double wedge case (Figure 26) uses two wedges with the same maximum elevations. Again, the transmitter is 10 meters above the ground and min range = 5 km, max range = 50 km, min height = 1 meter, max height = 1,001 meters MSL, number of ranges = 181, number of heights = 101, and the terrain profile in range in km and height in meters is (0, 0), (6.25, 0), (12.5, 450), (18.75, 0), (31.25, 0), (37.5, 450), (43.75, 0), and (50, 0).

For the two even wedges (now slightly higher and further from the transmitter) we notice some interesting differences in the models' behavior. Again, VTRPE gives results that demonstrate the presence of all of the correct physics are found in the algorithm. Interestingly, in the VTRPE results we see the energy reflected from the front of the first wedge and the diffraction pattern above the second wedge; features not seen in the other models. Unlike the first case, TIREM shows the deep shadow expected behind the first wedge. However, TIREM shows an anomaly emanating from the second wedge near the

shadow boundary. ITM also shows an unusual feature near the first shadow boundary. Further, the deep shadow behind the first wedge is not comparable with the PE results.

Figures 27 and 28 show the results of the two remaining test cases. The first shows the interaction with a rounded hill. As before, the transmitter is 10 meters above the ground, the min range = 5 km, max range = 50 km, min height = 1 meter, max height = 1,001 meters MSL, number of ranges = 181, number of heights = 101, and the terrain profile in range in km and height in meters is (0, 0), (18.75, 0), (20.312, 210), (21.875, 320), (23.4375, 375), (25, 390), (26.5625, 375), (28.125, 320), (31.25, 90), (32.8125, 0), and (50, 0).

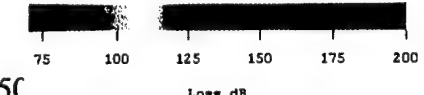
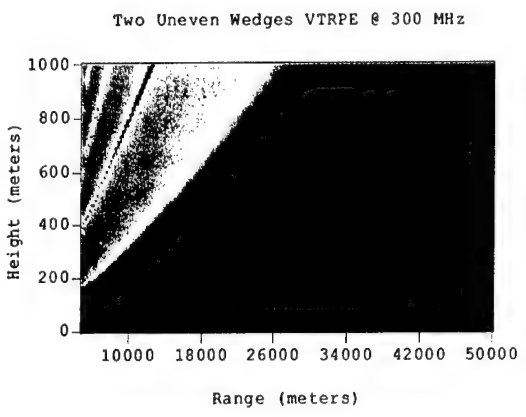
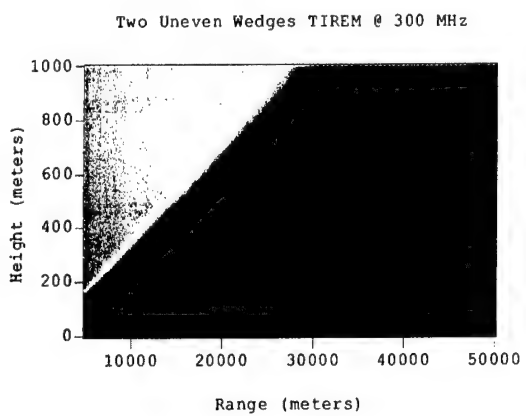
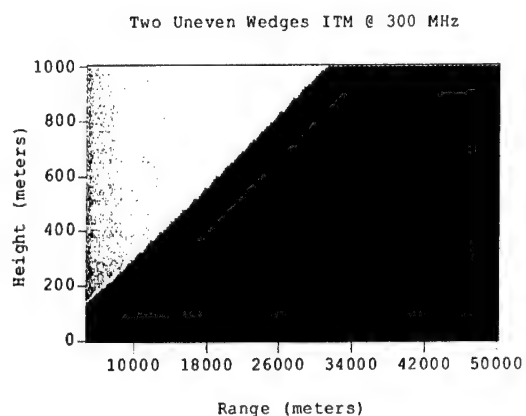
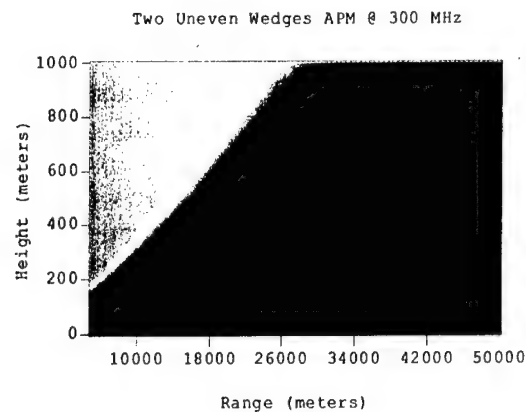
This test case challenges the models to represent a large rounded hill. Often this test will cause a model's diffraction search algorithms to give erroneous results. In fact, this test case demonstrates that TIREM may be unable to properly select the diffraction edges. Also because of the rounded transition to the shadow beyond the wedge, models that treat diffraction as a pure knife edge fail to give dark enough shadows near the ground behind the hill. Thus this test case illuminates ITM's method for computing diffraction and the resulting 30-40 dB difference between ITM and the PE models in the deep shadow. As has been observed in the previous test results, the PE models give physically reasonable results for this test case. Further VTRPE again models all of the propagation features expected by the physics governing this situation.

The final test case seeks to isolate diffraction from the other phenomena. In this case a transmitter at 1,278 meters MSL, vertical polarization, min range = 25 km, max range = 50 km, min height = 1,248 meters, max height = 3,248 meters for AGL and MSL, number of ranges = 201, number of heights = 101, the terrain profile in range in km and height in meters to (0, 0), (25, 1, 748), and (50, 0).

After reviewing the results from the previous test cases, the results for the final test are expected. Again the PE methods demonstrate the underlying physics very well. TIREM matches the PE methods quite well in the shadow region while ITM underestimates the loss in the deep shadow.

These test results confirm that correct modeling of the shadow boundary, reflection lobes, and deep shadows is required for JCS scenarios. After reviewing these test results and considering them together with the platform speed and environmental parameter resolution, it is clear that modeling the following features is less important than modeling the aforementioned first order features: small scale lobing in the illuminated diffraction region, smooth accurate transition from the illuminated to the shadow region, reflection structure in the shadow region, and reflection from the front faces of hills. These minor features do not have large loss variations and largely occur over small areas. Thus the time resolution of the simulation and corresponding spatial resolution render the second order effects inconsequential to JCS simulations.

Figure 32



50

Figure 33

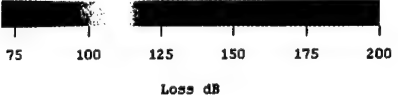
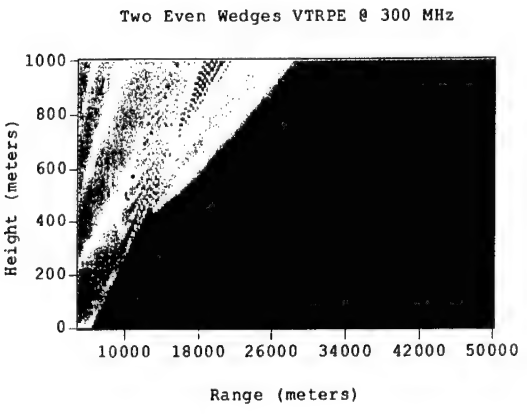
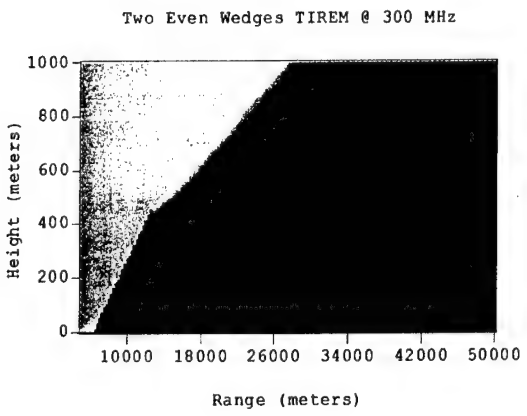
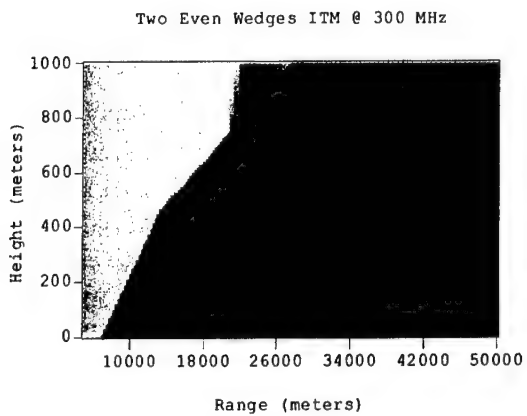
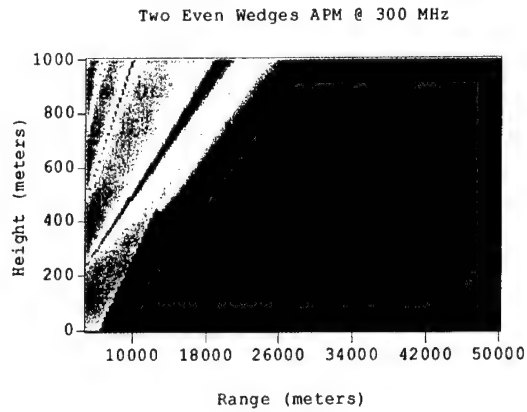


Figure 34

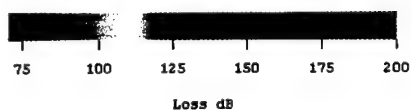
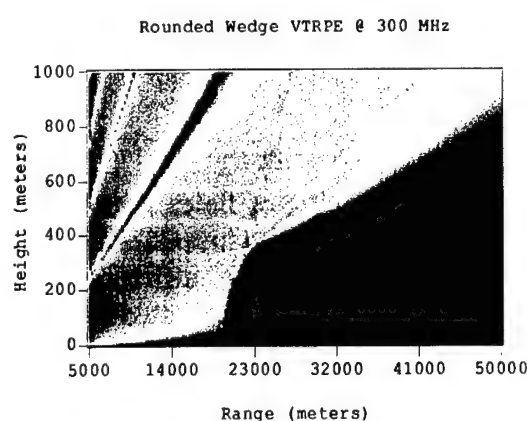
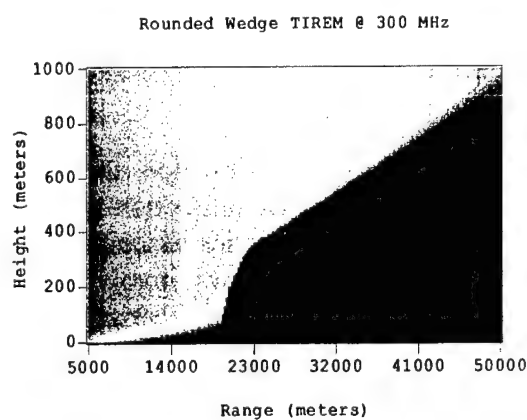
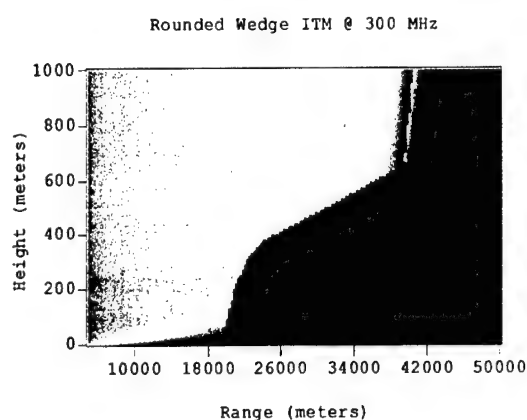
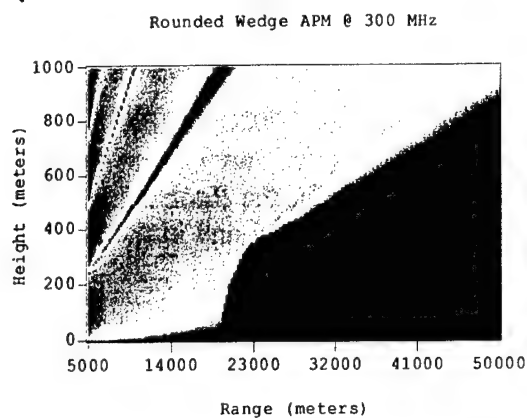
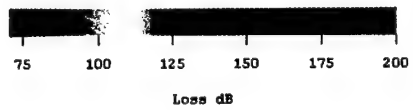
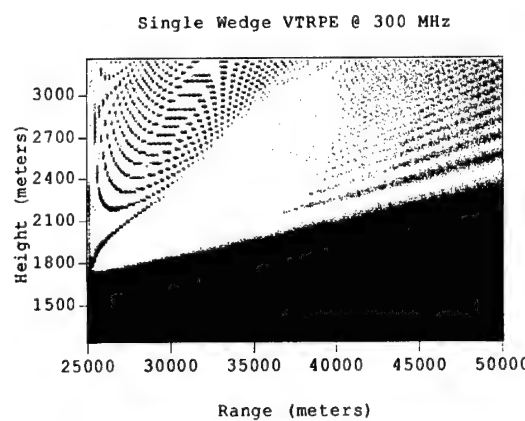
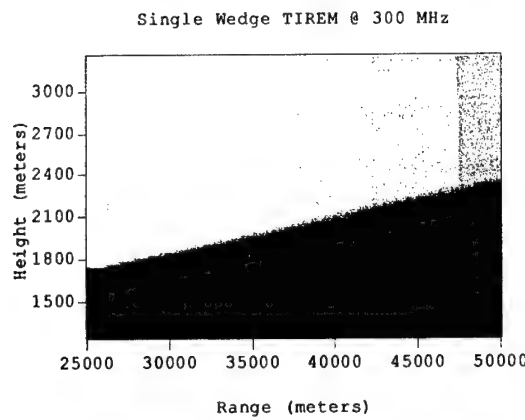
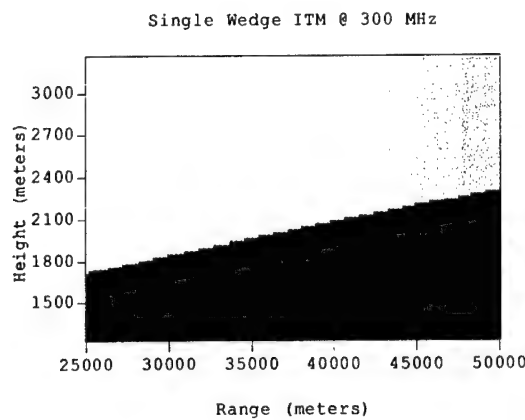
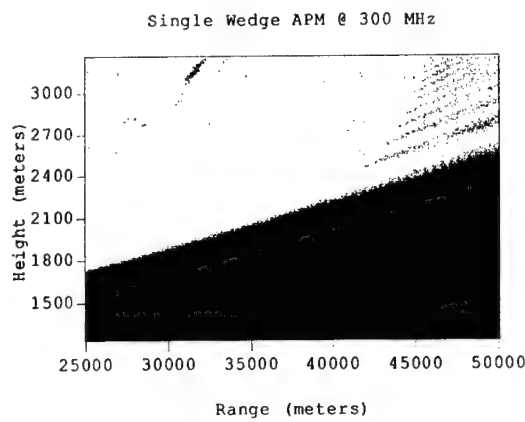


Figure 35



13.1.1.3. Run time comparisons

Using terrain data from Edwards Air Force Base, the run times for 36000 TIREM and ITM computations were compared. All of the following tests were run on an Intel Pentium 4 (3.06 Ghz) with 512MB RAM and a 512 KB Cache using the Redhat Linux 8.0 operating system. From the Sec® CPU 2000 benchmark data, chips found in the JCS have about 40% of the performance of the Pentium 4 used for this test.

	50 km	500 km
ITM	0.677 seconds	0.832 seconds
TIREM 3.14	1.256 seconds	10.156 seconds
TIREM 3.15	1.234 seconds	10.152 seconds

Although these tests were not completely comprehensive and the results preliminary, clearly ITM is much faster than TIREM. So once the core methods of these algorithms can be extracted and the blatant intolerable errors corrected, they can be written in the C programming language. The methods currently under development addressing this are discussed below.

13.1.2. Proposed methods and algorithm

13.1.2.1. Derivation and Discussion

This section will outline the theoretical motivation and practical justification for a number of features presently installed in the developing model. The first subsection will describe the method for enforcing continuity across the shadow boundaries associated with initial obstruction of inter-visibility and with higher order shadows involving multiple diffraction centers. Subsection [13.1.2.1.2] will present a qualitative description of a method employed to model specular reflections accompanying smooth earth attenuation of initially knife-edge diffracted fields. Subsection [13.1.2.1.3] will examine the multiplicity of theoretical and practical aspects of GTD and its accepted generalizations which contribute to its particular applicability to the present model. The final section will detail two representative auxiliary algorithmic constructs which have proven vital to the inevitable realization of the current objectives.

13.1.2.1.1. Initial and Multiple Knife Edge Shadow Boundary Continuity

A desirable feature of the proposed model is a continuous interfacing of fields initially propagated over a smooth earth which then encounter shadow boundaries introduced by irregular terrain features best modeled by GTD or single knife edge diffraction. Continuity across the shadow boundary of a smooth earth diffracted field attenuated by a knife edge can be enforced by a method similar to that found effective in enforcing continuity across the (second) shadow boundary of a double knife edge diffraction as

modeled by Epstein and Peterson [1]. Epstein and Peterson [1] model the double diffraction regions below the second shadow boundary as the product of two attenuations each calculated as an effective single knife edge attenuation in which the first knife edge serves as the source for the second. Thus in the Figure 29 curves R_{123} and R_{223} are associated with the conventional attenuation factors in which the first knife edge contributes the constant values α_{012} along curve R_{123} , below point C, and the second knife edge contributes the variable attenuation $\alpha_{12}(v_2)$ along curve R_{223} below transition region D.

Above the second shadow boundary the total attenuation may also be modeled as the product of two terms, the first of which, due to the first knife edge diffraction, A_1 is taken as $\alpha_{01}(v_1)$ along curve R_{112} above point C, with a lower limit set by its values at the second knife edge $A_1 = \alpha_{012}$. The second factor due to the diffraction by the second knife edge A_2 may be defined as one for values of the clearance ratio exceeding transition argument $v = 0.78$, above transition region D, and as the conventional second knife edge attenuation $A_2 = \alpha_{12}(v_2)$ for arguments less than 0.78, below transition region D. The activation of the second attenuation at .78 is continuous because the analytic attenuation $\alpha_{12}(v_2 = .78)$ is identical to the defined value of unity for values of v_2 exceeding .78. The loss increases continuously as a function of v_2 from an initial loss of 0 at the transition argument of $v_2 = .78$ to values of loss exceeding 0 for values of v_2 less than .78.

Proceeding similarly for the shadow boundary associated with a smooth earth diffracted field attenuated by a knife edge, the first attenuation factor is assigned its conventional value of α_0^{se} above point A along curve R_{001} and is assigned the limiting (constant) value of α_0^{se} below point A. The second attenuation factor, due to the first knife edge, is defined as 1 along curve R_{101} for arguments exceeding .78 (above transition region B) and is otherwise assigned its conventional single knife edge attenuation α_{01} along curve R_{112} , below transition region B. The success of this mechanism of enforcement of continuity across the smooth earth-knife edge shadow boundaries is apparent in the loss contour plots presented in this report.

13.1.2.1.2. Derivation of Terrestrial Specular Knife Edge Reflection

This section will present a qualitative description of a method employed to model specular reflections accompanying smooth earth attenuation of initially knife-edge diffracted fields. The smooth earth field propagation formulation of Norton [10] involves the summation of a direct ray and a reflected ray which is corrected for finite ground constants by a surface wave

$$E_D = \frac{e^{-ikr_1}}{4\pi r_1} + \frac{e^{-ikr_2}}{4\pi r_2} [DR + (1-R)f(P, B)] \quad (1)$$

Factoring out the direct ray, this may be written explicitly as the product of the direct ray and a smooth earth interference attenuation factor:

$$\frac{e^{-ikr_1}}{4\pi r_1} \left\{ 1 + e^{i\Delta} \frac{r_1}{r_2} [DR + (1-R)f(P,B)] \right\} \quad (2)$$

If the complex direct and reflected prefactors in Eq.(1) are replaced by smooth earth-knife edge attenuated field emanating from the first knife edge, one obtains

$$E^{(se,ke)}(v) = E^{ke}(v_1) + E^{ke}(v_2)[DR + (1-R)f(P,B)] \quad (3)$$

where quantities within the bracketed term are computed relative to the effective transmitter provided by the intervening knife edge, and where the Fresnel integral representation of knife edge attenuation assumes the form [8]

$$E^{(ke)}(v_i) = \frac{e^{-ikr_i}}{4\pi r_i} \left[\frac{1}{2} + \frac{e^{-i\pi/4}}{\sqrt{(2)}} \int_0^{v_i} e^{i\pi t^2} dt \right] \quad (4)$$

The Fresnel integrals appearing in this more general problem are not related by a multiplicative phase factor, but are rather explicit functions of the coordinates associated with the real and virtual receivers introduced by image theory and must therefore be evaluated independently as in Eq.(3). The above approximation is implemented by evaluating the knife edge attenuation at both real and virtual receivers, evaluating the bracketed expression in Eq.(3) with arguments consistent with a transmitter located at the intervening knife edge, and then adding the resulting generalized direct and reflected components. The inclusion of the surface wave component, appearing as the second term in Eq. (3), is expected to eliminate the inordinately high losses that often accompany the mutual cancellation of direct and reflected fields as modeled by a simple two ray specular reflection construction.

13.1.2.1.3. Justification for Selection of GTD and Extensions

This section will examine the appealing features inherent in GTD, its extension to multiple diffraction and its reinterpretation as the first term of an exact expansion. Techniques of geometrical optics applicable to classical diffraction originated by Keller [5] and refined by Kouyoumjian and Pathak [6] and practically adapted by Luebbers [7] and Holm [3][4] are appealing to the present objective and foundational to the example calculations presented in this report. The especially appealing features of GTD/UTD include its reduction to established exact first order approximations for both single and double knife edge configurations and its provision of a multiple diffraction algorithm for both knife edges and wedges which are identical to established first order terms for the more general multiple diffraction configurations.

Kouyoumjian and Pathak [6] show that their formulation of wedge diffraction, if applied to the special case of vanishing interior wedge angle, naturally reduces to Sommerfeld's solution for diffraction by a half plane. Also in the context of applications for single knife

edge diffraction and as applied to finite ground constants, Holm [4] has shown that a self-consistent modeling of the four UTD partial diffraction coefficients identifies a single term as being associated with a perfectly absorbing knife edge. This result is also consistent with the more general results of Sommerfeld for perfect conductivity of either polarization.

Extending this comparative study to established analytic results for two knife edges, in examining Holm's novel expression for multiple wedge diffraction as a sum of products of one dimensional Fresnel integrals, it becomes apparent that for the special case of two diffraction centers with zero interior wedge angle, Holm's expression reduces to Millington's exact derivation [9] of the correction of the Epstein Peterson model [1] for attenuation by two knife edges. In particular Millington shows that the Epstein Peterson expression is exact to within a factor of $\sin(\gamma)$ such that the magnitude of the doubly diffracted field is written

$$E^{2ke} = \alpha_{012}\alpha_{12}(v_2)\sin(\gamma) \quad (5)$$

where α_{012} and $\alpha_{12}(v_2)$ are attenuation factors associated with the first and second knife edges. Millington's essential correction of the Epstein Peterson formulation is the pre-factor multiplying the product of the single knife edge attenuations which in his notation is written

$$\sin(\gamma) = \left[\frac{b(a+b+c)}{(a+b)(b+c)} \right]^{1/2} \quad (6)$$

Converting to Holm's notation now by making the substitutions $a=r_1$, $b=r_2$ and $c=r_3$, one obtains

$$\sin(\gamma) = \left[\frac{r_2(r_1+r_2+r_3)}{(r_1+r_2)(r_2+r_3)} \right]^{1/2} \quad (7)$$

The analogous expression derived by Holm, in Eq.(9) of Reference [3], intended to also express double knife attenuation as a product of single knife edge attenuation factors, is

$$E = \left[\frac{r_T L_1 L_2}{r_1 r_2 r_3} \right]^{1/2} K_{012} K_{12} \quad (8)$$

Introducing the transformation expression

$$L_1 = \frac{r_1 r_2}{r_1 + r_2}$$

$$L_2 = \frac{r_2 r_3}{r_2 + r_3}$$

The Holm double knife attenuation prefactor becomes

$$A_{12} = \left[\frac{(r_1 + r_2 + r_3)(r_1 r_2)(r_2 r_3)}{r_1 r_2 r_3 (r_1 + r_2)(r_2 + r_3)} \right]^{1/2} \quad (9)$$

which reduces to

$$A_{12} = \left[\frac{(r_1 + r_2 + r_3)r_2}{(r_1 + r_2)(r_2 + r_3)} \right]^{1/2} \quad (10)$$

which is identical to Millington's expression , Eq. (6).

In view of the multiplicity of algorithms [2] proposed for modeling multiple knife edge diffraction, it is appealing that the established extension of GTD to multiple diffraction has been identified as the leading term of Vogler's exact series solution. The mechanical generalization of GTD to multiple diffraction when reduced to wedges with zero interior wedge angle provides a multiple knife edge algorithm with all the inherent advantages of GTD. Holm [3] has shown that GTD may be interpreted as the first term resulting from a rearrangement of Vogler's exact multiple knife edge expression and that the exact result may be obtained by including sufficiently many terms. Holm has also shown that the second term of his summation corresponds to slope diffraction which has been established as the leading second order correction of first order GTD. The provision by GTD of a multiple knife edge algorithm recognizable as the leading term of established exact expressions for multiple diffractions and recognition that the higher order terms themselves consist of one-dimensional integrals reinforces the perception of its desirability for the present purposes. Similar remarks apply to finite wedge angles and therefore an appealing continuity of formalism is realized in the generalization of multiple knife edge to multiple wedge diffraction. Thus GTD serves as first term of exact solution expressed as a summation which is especially relevant to previously intractable problems associated with overlapping shadow boundaries in that they may be solved by the simple inclusion of more terms.

13.1.2.1.4. Auxiliary Constructions Supportive of the Current Effort

This subsection will describe examples of supporting algorithms developed during the time frame of the current review period. The first portion of this subsection describes the complexity of proper computation of height gain functions inherent in smooth earth

propagation which has required numerical realization of the essential methods outline by Norton [10]. Finally, a method for eliminating troublesome interference variability is examined at the conclusion of this subsection.

Smooth earth algorithm of Norton with complete treatment of surface wave, height gain functions, and derivative conserving intermediate regime interpolation algorithm.

To assure proper treatment of those aspects of terrestrial propagation best modeled as diffraction over a smooth earth, the formulations of Norton [10] have been adapted in the time frame covered by this progress report to computational accessibility. Norton's form for the geometrical optics electric field propagated over a smooth planar earth is given by

$$E = \frac{e^{-ikr_1}}{4\pi r_1} \left\{ 1 + e^{i\Delta} \frac{r_1}{r_2} [R + (1-R)f(p,p)] \right\} \quad (11)$$

where Δ is the phase difference between direct and reflected ray paths $\Delta = 2\pi(r_2 - r_1)/\lambda$

For extended planar configurations with antennas close to the ground, the reflection coefficient approaches -1, and the above planar earth formulation as modeled by Norton approaches an intermediate asymptotic form associated with complete mutual interference of direct and reflected waves to define a surface wave which must be refined by height gain factors:

$$E(r) = \frac{e^{-ikr_1}}{4\pi r_1} [2f(p,b)Z(q_2)] \quad (12)$$

where $Z(q_i); i = 1,2$ is the height gain factor associated with the transmitter/receiver and where q_1 and q_2 are scaled antenna heights normalized by ground constant parameters. For sufficiently elevated antennas, the argument dependence of the height gain factors must be generalized to include another argument, the ground constant and frequency dependent parameter K such that the above equation is written

$$E(r) = \frac{e^{-ikr_1}}{4\pi r_1} [2f(p,b)Z(q_1, K)Z(q_2, K)] \quad (13)$$

For sufficiently elevated antenna, the two physical form of the diffracted field are unified in a single theoretical formulation

$$E(r) = \frac{e^{-ikr_1}}{4\pi r_1} \left\{ 1 + e^{i\Delta} \frac{r_1}{r_2} [R'D + (1-R')f(P,B)] \right\} \quad (14)$$

where primes indicate dependence upon spherical earth geometry and where D is a divergence factor not explicitly present in the planar earth formulation. The height gain factors in the extended planar surface wave and in the more general spherical earth formulation may be identified as factors that appear in Bremmer's exact solution which admits to a Hankel approximation involving solution of the root generating equation

$$H_1^{1/3}(\xi) = (3\xi)^3 e^{i(-b/2+5\pi/12)} H_1^{2/3}(\xi) \quad (15)$$

where $H_1^v(\xi)$ is the complex Hankel function of the first kind of real order v and $\xi = \sqrt{(-2r_0)}$. The arguments q_i and K of the height gain factors $Z(q_i, K)$ are functions of the complex quantity, r_0 appearing in the above equation which must be solved to properly compute the vital height gain factors in Norton's formulation. The above formulations are valid within a restricted range of the horizon dictated by the limits of geometrical optics such that the proper form beyond these limits is computed as an interpolating function between the geometrical optical limits and the final diffracted form approximated by the first terms of the Bremmer series. Within the time frame covered by this progress report, the graphical methods of Norton have been mathematically transformed for computational accessibility, the proper special functions for computing the surface wave have been collected and numerical iterative solutions to the complex Hankel root-generating equation have been developed to compute the complex quantities upon which the arguments of the height gain functions depend. The success of the implementations is apparent from the replication of Figures 13-15 in Norton's paper.

Elimination of numerical precision variability associated with superposition of UTD direct and diffracted components with essential first order small argument phase difference expression at overlapping shadow boundaries.

Above the shadow boundaries, the formalism of GTD requires that the direct ray serving as source to the diffraction center is added to the diffracted ray itself. In the approach to shadow boundary from the illuminated half-plane, the diffracted ray approaches a form which may be identified as -1/2 the direct ray and the superposition of the two leads to a total field which is (1/2) times the direct ray for the characteristic 6 dB loss. Below the shadow boundary, the direct ray no longer contributes and the diffraction formalism imposes a change in sign on the diffracted ray such that the total ray is purely diffracted and of exactly the same magnitude as the total field infinitesimally above the shadow boundary. Coexisting with the delicacies of field continuity across the shadow boundary is a possibility for an undesirable numerical variability resulting from the addition of the direct and diffracted rays which is attributable to small phase differences of the two wave forms. The interference factor of the direct and diffracted components can be represented by

$$E_D = \frac{e^{-ikr_1}}{4\pi r_1} [1 + (r / \rho') DA e^{-ik(\rho + \rho' - r)}] \quad (16)$$

The phase factor $r^{-ik(\rho+\rho'-r)}$ essentially involves the subtraction of one quantity, r , the magnitude of the direct ray from the sum of two quantities $(\rho + \rho')$ to produce a phase difference factor which in fact vanishes at the shadow boundary. The numerical variability (noise) resulting from taking the difference of two relatively large quantities of vanishing difference was solved by examining the geometrical origins of the magnitude difference term suggested by the equation

$$r = \rho - \rho' \quad (17)$$

Extracting square magnitudes, one obtains

$$r^2 = \rho^2 + \rho'^2 - 2\rho\rho' \cos(\phi - \phi') \quad (18)$$

In the vicinity of the shadow boundary $\phi - \phi' = \pi + \varepsilon$ and the above equation may be rewritten as

$$r^2 = \rho^2 + \rho'^2 - 2\rho\rho' \cos(\pi + \varepsilon) \quad (19)$$

Expanding the cosine function for small displacements ε about π , one obtains $-1 + \varepsilon^2 / 2$ and the above equation becomes

$$r^2 = \rho^2 + \rho'^2 - 2\rho\rho'(-1 + \varepsilon^2 / 2) \quad (20)$$

$$r^2 = \rho^2 + \rho'^2 - 2\rho\rho' - \rho\rho'\varepsilon^2$$

$$r^2 = (\rho + \rho'^2) - \rho\rho'\varepsilon^2$$

$$r = \left[(\rho + \rho')^2 - \rho\rho'\varepsilon^2 \right]^{1/2}$$

Expanding the radical for $(\rho\rho'\varepsilon^2) \ll (\rho + \rho')^2$, one obtains

$$r = \rho + \rho' - \frac{\rho\rho'}{2(\rho + \rho')} \varepsilon^2 \quad (21)$$

and the quantity of interest becomes

$$\rho + \rho' - r = \frac{\rho\rho'}{2(\rho + \rho')} \varepsilon^2 \quad (22)$$

and Eq. [16] may be written

$$E_D = \frac{e^{-ikr_1}}{4\pi r_1} \left[1 + \left(r / \rho' \right) D A e^{-ik\delta r} \right] \quad (23)$$

where

$$\delta r = \rho + \rho' = \frac{\rho\rho'}{2(\rho + \rho')} \varepsilon^2 \quad (24)$$

Eq. (23) is of course exact and the approximation in Eq. (24) is only required in the vicinity of the shadow boundary and was found to effectively eliminate numerical variability (noise) in plots of the interfering fields.

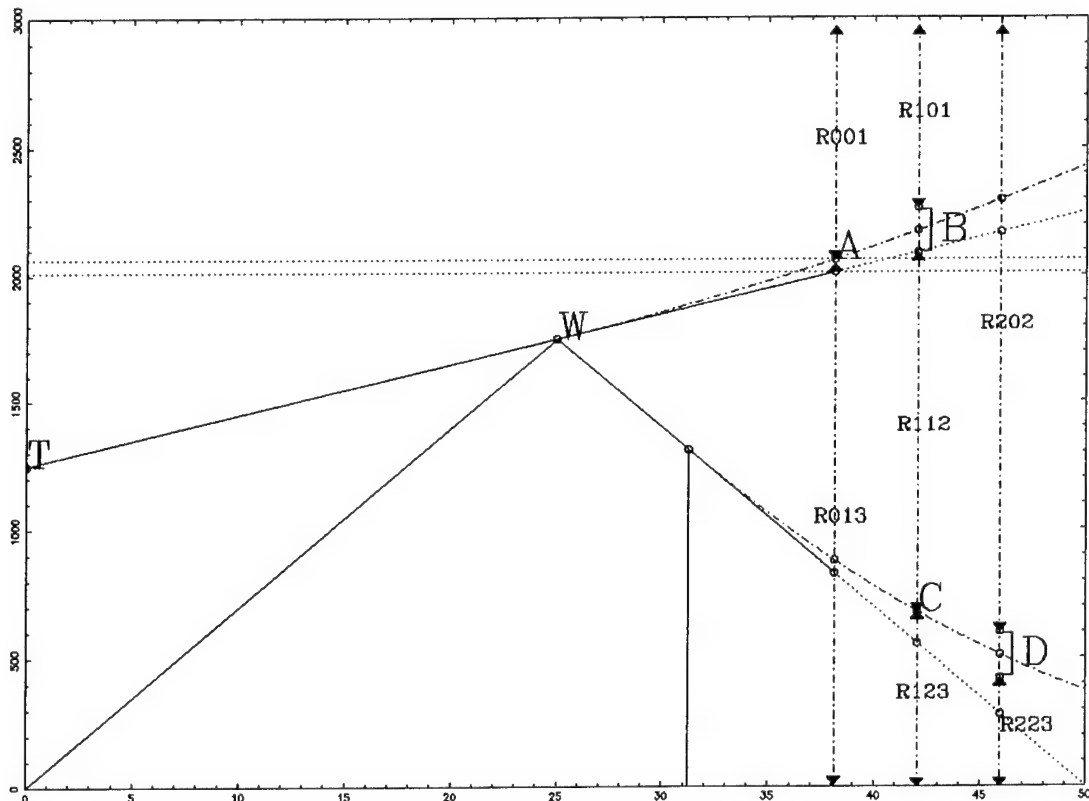


Figure 36

13.1.2.2. Comparison with other models

A graphical comparison of path loss contour plots in the vertical propagation plane obtained from four established propagation models and of the proposed model in its current state of development appears in Figure 37 and Figure 38. The most striking difference among the coverage presentations in the lit region is the relative presence of

the fine interference structure as seen in APM and VTRPE. Though striking, such differences are usually merely indicative of whether the model in question suppresses superposition of direct and ground specular reflections. The profile essentially involves three perfectly absorbing knife edges in the first, third and fourth positions which create three successive shadows asymptotically and a fourth knife edge in the second position which is only a partial mask for the for the third knife edge and casts only a finite shadow. A vertical excursion at great distances for such a configuration should encounter three shadow boundaries and should exhibit a monotonic increase in loss upon traversing the first shadow boundary from above. This behavior is indeed exhibited in APM, VTRPE, and our proposed model, whereas ITM exhibits precipitous discontinuities at the first and second shadow boundaries and fails to detect a third shadow boundary and the TIREM exhibits a misplaced region of excessive loss in the vicinity of the second shadow boundary.

A horizontal excursion proceeding from the transmitter for such a terrain profile is expected to exhibit a monotonic increase in loss upon penetrating the first shadow boundary and to then experience two additional shadow boundaries if at an elevation greater than the third knife edge and one additional shadow if at a lesser elevation. These features are again exhibited in the APM, VTRPE, and the proposed model whereas TIREM again has difficulties in the second shadow for low and high elevation horizontal excursions and ITM model exhibits non-physically severe losses across both interpretations of its first shadow which curiously intersect at the third knife edge.

Thus unlike TIREM and ITM, our model agrees well with the more rigorous results found in APM and VTRPE with the advantage that it's run time are comparable with TIREM and ITM.

Figure 37

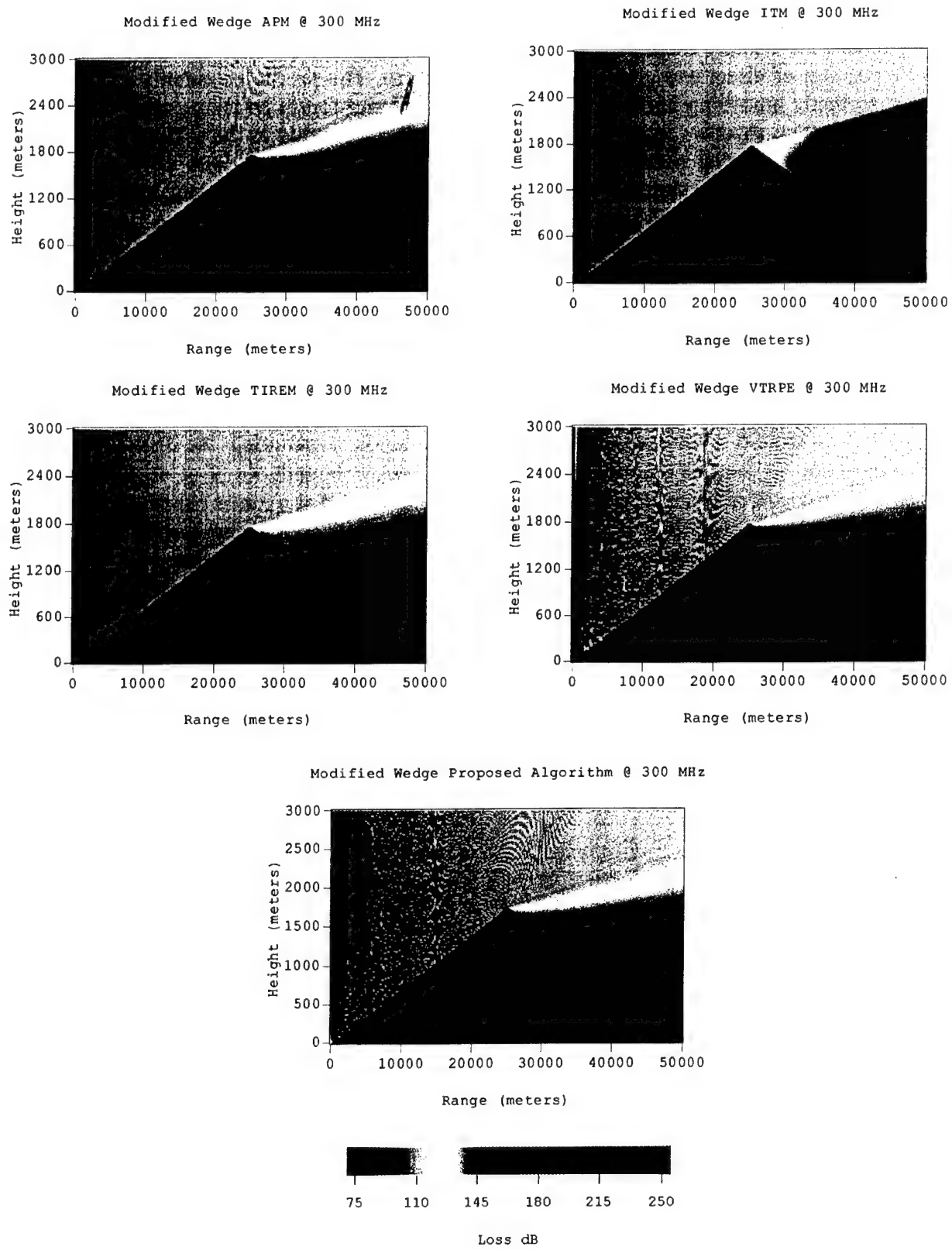
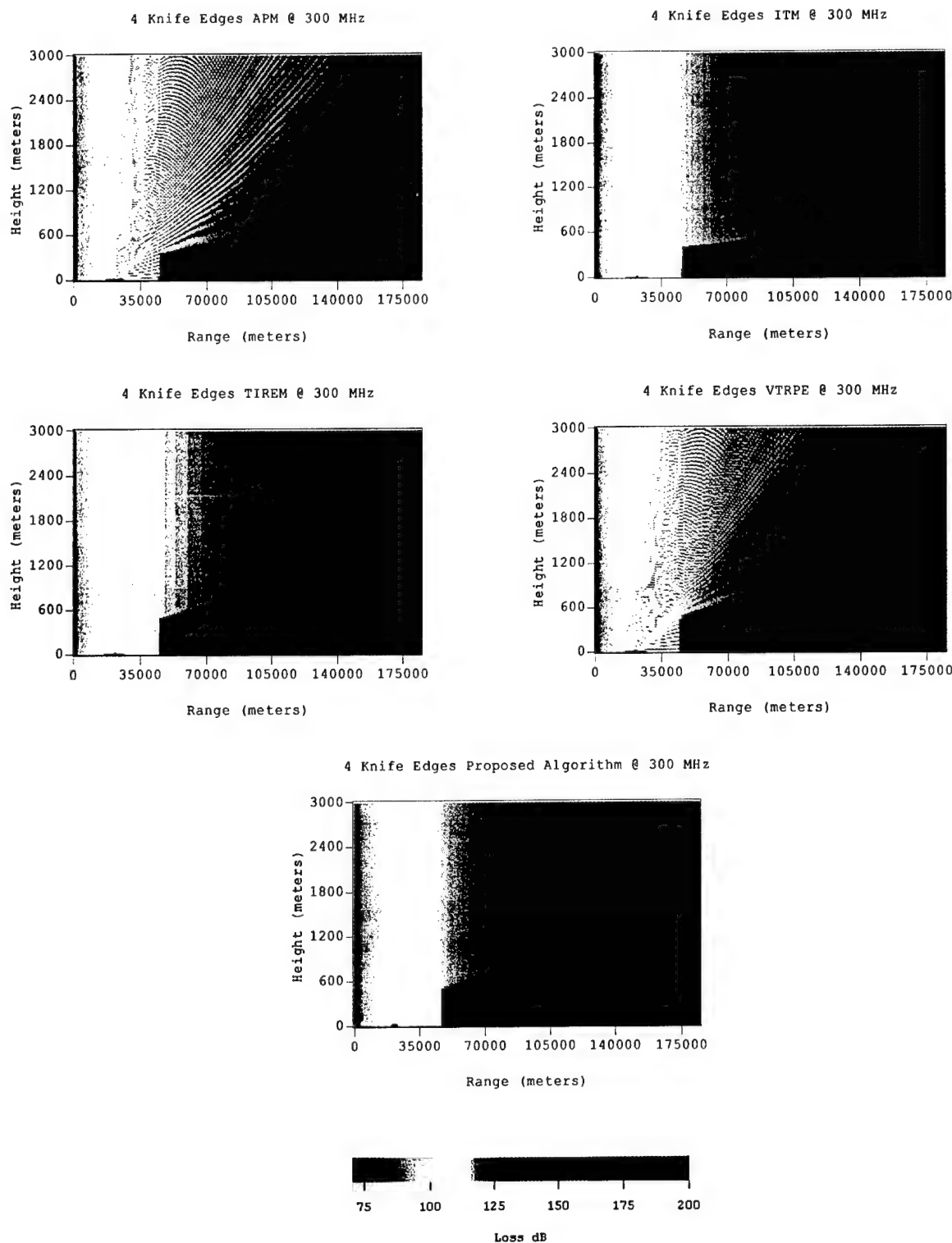


Figure 38



14. Bibliography

- [1]. Epstein, Jess, Peterson, Donald W., "An Experimental Study of Wave Propagation at 850 MC," *Proceedings of the I.R.E.*, 41 (5), pp. 595-611, May 1953.
- [2]. Giovaneli, Carlos Lopez, "An Analysis of Simplified Solutions for Multiple Knife-Edge Diffraction," *IEEE Transactions on Antennas and Propagation*, AP-32 (3), pp. 297-301, March 1984.
- [3]. Holm, P. D., "UTD-Diffraction Coefficients for Higher Order Wedge Diffracted Fields," *IEEE Transactions on Antennas and Propagation*, 44 (6), pp. 879-888, June 1996.
- [4]. Holm, P. D., "A New Heuristic Diffraction Coefficient for Nonperfectly Conducting Wedges," *IEEE Transactions on Antenna and Propagation*, 48(8), pp. 1211-1219, 2000.
- [5]. Keller, J.B., "Geometric Theory of Diffraction," *J. Optical Society of America*, 52, pp. 116-130, 1962.
- [6]. Kouyoumjian, Robert G., Pathak, Prabhakar H., "A Uniform Geometrical Theory of Diffraction for an Edge in a Perfectly Conducting Surface," *Proceedings of the IEEE*, 62 (11), pp. 1448-1461, November, 1974.
- [7]. Luebbers, R.J., "A Heuristic UTD Slope Diffraction Coefficient for Rough Lossy Wedges," *IEEE Transactions on Antennas and Propagation* 37(2), pp. 206-211, 1989.
- [8]. Meeks, M.L., *it Radar Propagation at Low Altitudes*, Artech House, pp. 27-32, 1982
- [9]. Millington, G., Hewitt, R., Immirzi, F. S., "Double Knife-Edge Diffraction in Field-Strength Predictions," *The Institution of Electrical Engineers*, 507 E., pp. 419-429, March, 1962.
- [10]. Norton, K.A., "The Calculation of Ground Wave Field Intensity Over a Finitely Conducting Spherical Earth," *Proceedings of the I.R.E.* 29(12), pp. 623-639, 1941.
- [11]. Tukizi, O., "Diffraction Theory of Tropospheric Propagation Near and Beyond the Radio Horizon," *IRE Transactions on Antennas and Propagation*, AP-7 (3), pp. 261-273, July, 1959.
- [12]. Logan, N. A., "Comments on "Diffraction Theory of Tropospheric Propagation Near and Beyond the Radio Horizon"," *IRE Transactions on Antennas and Propagation*, AP-10 (1), pp. 98-99, January, 1962.
- [13]. Rice, S. O, "Diffraction of Plane Radio Waves by a Parabolic Cylinder," *The Bell System Technical Journal*, 33 (2). pp. 417-505, March, 1954.

- [14]. Wait, James R., Conda, Alyce M., "On the Computation of Diffraction Fields for Grazing Angles," *Electromagnetic Wave Propagation*, pp. 661-671, 1960.
- [15]. Anderson, L. J., Trolese, L. G., Weisbrod, S., "Simplified Method for Computing Knife-edge Diffraction in the Shadow Region." *Electromagnetic Wave Propagation*, pp. 209-215, 1960.
- [16]. Shatz, M. P., Polychronopoulos, G. H., "An Improved Spherical Earth Diffraction Algorithm for SEKE" Massachusetts Institute of Technology, pp. 1-40, April, 1988.
- [17]. Wait, James R., Conda, Alyce M., "Diffraction of Electromagnetic Waves by Smooth Obstacles for Grazing Angles," *Journal of Research of the National Bureau of Standards*, pp. 181-197, March, 1959.
- [18]. Vogler, Lewis E., "An attenuation function for multiple knife-edge diffraction," *Radio Science*, 17 (6), pp. 1541-1546, November/December 1982.
- [19]. Barsis, A. P., Kirby, R. S., "VHF and UHF Signal Characteristics Observed on a Long Knife-Edge Diffraction Path," *Journal of Research National Bureau of Standards*, 65D (5), pp. 437-448, September/October 1961.
- [20]. McPetrie, J. S., Saxton, J. A., "Diffraction of Ultra-Short Radio Waves," *Nature*, 150 (3801), pp. 292, September, 1942.
- [21]. Vogler, L. E., "Calculation of Groundwave Attenuation in the Far Diffraction Region," *Radio Science*, 68D (7), pp. 819-828, July, 1964.
- [22]. Wait, James. R., Spies, Kenneth P., "On the Diffraction by a Knife-Edge Obstacle on a Conducting Earth," *Radio Science*, 3 (12), pp. 1179-1181, December, 1968.
- [23]. Crysdale, J. H., Day, J. W., Cook, W. S., Psutka, M. E., Robillard, P. E., "An Experimental Investigation of the Diffraction of Electromagnetic Waves by a Dominating Ridge," *IRE Transactions on Antennas and Propagation*, AP-5 (2), pp. 203-210, April, 1957.
- [24]. Hong, Soonsung, "Asymptotic Theory of Electromagnetic and Acoustic Diffraction by Smooth Convex Surfaces of Variable Curvature," *Journal of Mathematical Physics*, 8 (6), pp. 1223-1232, June, 1967.
- [25]. Neugebauer, H. E., Bachynski, M. P., "Diffraction by Smooth Cylindrical Mountains," *Proceedings of the IRE*, 46 (9), pp. 1619-1627, September, 1958.
- [26]. De Assis, Mauro S., "A Simplified Solution to the Problem of Multiple Diffraction over Rounded Obstacles," *IEEE Transactions on Antennas and Propagation*, AP-19 (2), pp. 292-295, March, 1971.

- [27]. Kortunov, V. A., Strel'Nikov, Yu. M., Kivva. F. V., "On the Effect of Refraction on the Propagation of Meter Radio Waves Near the Diffraction Horizon," *Soviet Journal of Communications Technology and Electronics*, 35 (10), pp. 72-76, 1990.
- [28]. Deygout, Jacques, "Multiple Knife-Edge Diffraction of Microwaves," *IEEE Transactions on Antennas and Propagation*, AP-14 (4), pp. 480-489, July, 1966.
- [29]. Anders, Jon, "On the Accuracy of the Uniform Geometrical Theory of Diffraction Close to a 90 degree Wedge," *IEEE Transactions on Antennas and Propagation*, AP-27 (5), pp. 704-705, September, 1979.
- [30]. Meeks, M. L., "A Propagation Experiment Combining Reflection and Diffraction," *IEEE Transactions on Antennas and Propagation*, AP-30 (2), pp. 318-321, March, 1982.
- [31]. Luebbers, Raymond J., "Propagation Prediction for Hilly Terrain Using GTD Wedge Diffraction," *IEEE Transactions on Antennas and Propagation*, AP-32 (9), pp. 951-955, September, 1984.
- [32]. Barsis, A. P., Kirby, R. S., "VHF and UHF Signal Characteristics Observed on a Long Knife-Edge Diffraction Path," *Journal of Research of National Bureau of Standards Radio Propagation*, 65D (5), pp. 437-448, September/October 1961.
- [33]. Barsis, A. P., Kirby, R. S., "VHF and UHF Signal Characteristics Observed on a Long Knife-Edge Diffraction Path," *National Bureau of Standards Report*, Report # 6751, pp. 1-Figure 16, March, 1961.
- [34]. Saunders, S. R., Bonar, F. R., "Explicit Multiple Building Diffraction Attenuation Function for Mobile Radio Wave Propagation," *Electronics Letters*, 27 (14), pp. 1276-1277, July, 1991.
- [35]. Wait, James R., "Comments on the "Application of Diffractions by Convex Surfaces to Irregular Terrain Situations: by H. T. Dougherty and L. J. Maloney," *Radio Science*, 3 (6), pp. 638, June, 1968.
- [36]. Vogler, Lewis E., "Radio wave diffraction by a rounded obstacle," *Radio Science*, 20 (3), pp. 582-590, May/June 1985.
- [37]. Whitteker, J. H., "Fresnel-Kirchhoff theory applied to terrain diffraction problems," *Radio Science*, 25 (5), pp. 837-851, September/October 1990.
- [38]. Dougherty, H. T., Maloney, L. J., "Application of Diffractions by Convex Surfaces to Irregular Terrain Situations," *Radio Science Journal of Research NBS/USNC-USRI*, 68D (2), pp. 239-250, February, 1964.
- [39]. Dougherty, Harold T., Wilkerson Robert E., "Determination of Antenna Height for Protection against Microwave Diffraction Fading," *Radio Science*, 2 (2), pp. 161-165, February, 1967.

- [40]. Luebbers, Raymond J., "Finite Conductivity Uniform GTD Versus Knife Edge Diffraction in Prediction of Propagation Path Loss," *IEEE Transactions on Antennas and Propagation*, AP-32 (1), pp. 70-76, January, 1984.
- [41]. Pogorzelski, R. J., "A note on some common diffraction link loss models," *Radio Science*, 17 (6), pp. 1536-1540, November/December 1982.
- [42]. Whitteker, J. H., "A series solution for diffraction over terrain modeled as multiple bridged knife edges," *Radio Science*, 28 (4), pp. 487-500, July/August, 1993.
- [43]. Booker, H. G., Walkinshaw, W., "The Mode Theory of Tropospheric Refraction and its Relation to Wave-Guides and Diffraction," *Meteorological Factors in Radio-Wave Propagation*, pp. 80-127, April, 1946.
- [44]. Pathak, P. H., "An asymptotic analysis of the scattering of plane waves by a smooth convex cylinder," *Radio Science*, 14 (3), pp. 419-435, May/June 1979.
- [45]. Pathak, Prabhakar, H., Burnside, Walter D., Marhefka, Ronald J., "Uniform GTD Analysis of the Diffraction of Electromagnetic Waves by a Smooth Convex Surface," *IEEE Transactions on Antennas and Propagation*, AP-28 (5), pp. 631-641, September 1980.
- [46]. Kouyoumjian, R. G., "The Geometrical Theory of Diffraction and Its Application," *Numerical and Asymptotic Techniques in Electromagnetics*, New York 1975.
- [47]. Pathak, Prabhakar H., Kouyoumjian, Robert G., "An Analysis of the Radiation from Apertures in Curved Surfaces by the Geometrical Theory of Diffraction," *Proceedings of the IEEE*, 63 (11), pp. 1438-1447, November 1974.
- [48]. Wait, James R., "Radiation from a Vertical Antenna Over a Curved Stratified Ground," *Journal of Research of the National Bureau of Standards*, 56 (4), pp. 237-244, April 1956.
- [49]. Dougherty, H. T., "Radio wave propagation for irregular boundaries," *Radio Science*, 4 (11), pp. 997-1004, November 1969.
- [50]. Dougherty, H. T., "The application of stationary phase to radio propagation for finite limits of integration," *Radio Science*, 5 (1), pp. 1-6, January 1970.
- [51]. Ayasli, Serpil, "SEKE: A Computer Model for Low Altitude Radar Propagation Over Irregular Terrain," *IEEE Transactions on Antennas and Propagation*, AP-34 (8), pp. 1013-1023, August 1986.
- [52]. Meeks, M. L. "VHF Propagation over Hilly, Forested Terrain," *IEEE Transactions on Antennas and Propagation*, AP-31 (3), pp. 483-489, May 1983.
- [53]. Schelleng, J. C., Burrows, C. R., Ferrell, E. B., "Ultra-Short-Wave Propagation," *Proceedings of the Institute of Radio Engineers*, 21 (3), pp. 427-463, March 1933.

- [54]. Dougherty, H. T., "An expansion of the Helmholtz integral and its evaluation," *Radio Science*, 4 (11), pp. 991-995, November 1969.
- [55]. Eliades, D. E., Sharples, P. A., Mehler, M. J., Howell, R., "Comparison of Different Methods for Modelling Terrain Diffraction Loss at S.H.F.," University of Birmingham, U.K., British Telecom Research Laboratories, U.K., pp. 377-379.
- [56]. Bullington, Kenneth, "Radio Propagation Fundamentals," *Bell Syst. Tech. J.*, 36, pp. 593-626, May 1957.
- [57]. Grosskopf, Rainer, "Comparison of Different Methods for the Prediction of the Field Strength in the VHF Range," *IEEE Transactions on Antennas and Propagation*, AP-35 (7), pp. 852-859, July 1987.
- [58]. Uslenghi, P. L. E., "Geometrical Optics Exact Solutions for Two Classes of Dielectric Wedge Structures," *IEEE Transactions on Antennas and Propagation*, 44 (1), pp. 129, January 1996.
- [59]. Kouyoumjian, R. G., Pathak, P. H., "The Dyadic Diffraction Coefficient for a Curved Edge," *National Aeronautics and Space Administration*, CR-2401, June 1974.
- [60]. Hutchins, David L., Kouyoumjian, Robert G., "Asymptotic Series Describing the Diffraction of a Plane Wave by a Wedge," *Defense Technical Information Center*, 2183-3, pp. 1-149, December 1969.
- [61]. Luebbers, Dr. Raymond J., Chamberlin, Dr. Kent A., "Evaluation of a Terrain-Sensitive, Propagation Path Loss Model Based Upon the Geometrical Theory of Diffraction," Modified for Finite Conductivity and Local Surface Roughness," pp. 1-140.
- [62]. Chamberlin, Kent A., Luebbers, Raymond J., "An Evaluation of Longley-Rice and GTD Propagation Models," *IEEE Transactions on Antennas and Propagation*, AP-30 (6), pp. 1093-1098, November 1982.
- [63]. Luebbers, Raymond J., Foose, William A., Reyner, Gregory, "Comparison of GTD Propagation Model Wide-Band Path Loss Simulation with Measurements," *IEEE Transactions on Antennas and Propagation*, 37 (4), pp. 499-505, April 1989.
- [64]. Bisceglia, B., Franceschetti, G., Mazzarella, G., Pinto, I. M., Savarese, C., "Program for Automatic Ray Tracing and Path-Loss Evaluation of Radio Links Over Two-Dimensional Piecewise-Linear Terrain Profiles," *IEEE Transactions on Antennas and Propagation*, 36 (10), pp. 1499-1500, October 1988.
- [65]. Lee, S. W., Cramer, Paul Jr., Woo, Kenneth, Rahmat-Samii, Yahya, "Diffraction by an Arbitrary Subreflector: GTD Solution," *IEEE Transactions on Antennas and Propagation*, AP-27 (3), pp. 305-316, May 1979.

- [66]. Luebbers, Raymond J., "A Semiblind Test of the GTD Propagation Model for Reflective Rolling Terrain," *IEEE Transactions on Antennas and Propagation*, 38 (3), pp. 403-405, March, 1990.
- [67]. Glassner, Andrew S., "Ray Tracing for Realism," *State of the Art*, pp. 263-271, December 1990.
- [68]. Chillingworth, David R. J., Danesh-Narouie, G. R., Westcott, Bryan S., "On Ray-Tracing Via Caustic Geometry," *IEEE Transactions on Antennas and Propagation*, 38 (5), pp. 625-632, May 1990.
- [69]. Schneider, Michael, Luebbers, Raymond J., "A General, Uniform Double Wedge Diffraction Coefficient," *IEEE Transactions on Antennas and Propagation*, 30 (1), pp. 8-14, January, 1991.
- [70]. Bachynski, M. P., "Propagation at Oblique Incidence Over Cylindrical Obstacles," *Journal of Research of the National Bureau of Standards*, 64D (4), pp. 311-315, July-August 1960.
- [71]. Baum, Carl E., "Scattering from Cones, Wedges, and Half Spaces," *Interaction Notes*, Note 493, pp. 1-22, May 1993.
- [72]. Baum, Carl E., "Scattering from Finite Wedges and Half Spaces," *Interaction Notes*, Note 495, pp. 1-31, May 1993.
- [73]. Bremmer, H., "Applications of Operational Calculus to Ground-Wave Propagation, Particularly for Long Waves," *IRE Transactions on Antennas and Propagation*, pp. 267-272, July 1958.
- [74]. de Assis, M. S., "The Problem of Multiple Diffraction over Rounded Obstacles," *IEEE Transactions on Antennas and Propagation*, AP-19 (2), pp. 292-295, March 1971.
- [75]. Dougherty, H. T., Dutton, E. J., "Quantifying the Effects of Terrain for VHF and Higher Frequency Application," U.S. Department of Commerce, 86-200, pp. 1-50, July 1986.
- [76]. Sailors, D. R., Barrios, A. E., Patterson, W. L., Hitney, H. V., "Advanced Propagation Model Computer Software Configuration Item Documents," Space and Naval Warfare Systems Center, Technical Document 3033, August 1998.
- [77]. Eppink, D., and Kuebler, W., TIREM/SEM Handbook, ECAC-HDBK-93-076, 1993.
- [78]. Sciandra, Ronald M., TIREM/SEM Programmer's Reference Manual, ECAC-CR-90-039, July 1990.

- [79]. Ryan, F. J., *User's Guide for the VTRPE (Variable Terrain Radio Parabolic Equation) Computer Model*, Naval Command, Control, and Ocean Surveillance Center Technical Document 1456, Revision C, October 1998.
- [80]. Ryan, F. J. Analysis of Electromagnetic Propagation Over Variable Terrain Using the Parabolic Wave Equation, Ocean and Atmospheric Sciences Division, Technical Report 1453, October 1991.
- [81]. Hufford, G. A., Longley, A. G., and Kissick, W. A., A Guide to the Use of the ITS Irregular Terrain Model in the Area Prediction Mode, NTIA Report 82-100, Springfield, Virginia: U.S. Department of Commerce, National Technical Information Service, 1982.
- [82]. Hufford, George, The ITS Irregular Terrain Model, version 1.2.2 The Algorithm, National Telecommunications and Information Administration Institute for Telecommunications Sciences.
- [83]. Barrios, Amalia E., "Parabolic Equation Modeling in Horizontally Inhomogeneous Environments", *IEEE Transactions on Antennas and Propagation*, 40 (7), pp. 791-797, July, 1992.
- [84]. Craig, K. H., Barrios, A. E., "Comparison of radiowave propagation parabolic equation computer implementations," NRPP Research, 136, pp. 1-35, December, 1992.
- [85]. Barrios, Amalia E., "A Terrain Parabolic Equation Model for Propagation in the Troposphere," *IEEE Transactions on Antennas and Propagation*, 42 (1), pp. 90-98, January, 1994.
- [86]. Fast, S. A. and Ryan, F. J., "A Numerical Comparison of Wedge Diffraction Using Uniform Geometrical Theory of Diffraction and Parabolic Equation Methods," *IEEE A&P Symposium*, 1996.
- [87]. Ryan, F. J. and Fast, S. A., "Prediction of HF Communication Links in Littoral Environments Using Parabolic Equation Methods," *Proceedings of the Electromagnetic/Electro-Optics Prediction Requirements & Products Symposium*, 1997.
- [88]. Deygout, Jacques, "Correction Factor for Multiple Knife Edges Diffraction", *IEEE Transaction on Antennas and Propagation* 39(8), 1256-1258 (1991).